

Role of neutral transport in aspect ratio dependent plasma etching of three-dimensional features

Chad M. Huard^{a)}

Department of Electrical Engineering and Computer Science, University of Michigan, 1301 Beal Ave., Ann Arbor, Michigan 48109-2122

Yiting Zhang,^{b)} Saravanapriyan Sriraman,^{c)} and Alex Paterson^{d)}

Lam Research Corp., 4650 Cushing Parkway, Fremont, California 94538

Mark J. Kushner^{e)}

Department of Electrical Engineering and Computer Science, University of Michigan, 1301 Beal Ave., Ann Arbor, Michigan 48109-2122

(Received 29 October 2016; accepted 21 December 2016; published 17 January 2017)

Fabrication of semiconductor devices having three-dimensional (3D) structures places unprecedented demands on plasma etching processes. Among these demands is the frequent need to simultaneously etch features with a wide variety of aspect ratios (AR) on the same wafer. Many plasma etching processes exhibit aspect ratio dependent etching (ARDE)—different etch rates for features that have different aspect ratios, usually slower for larger AR. Processes subject to ARDE require over-etch to clear the larger AR features, which increases the need for high selectivity and low damage. Despite these issues, the physical processes which contribute to ARDE are not well understood. In this paper, results are discussed from a computational investigation on the root causes of ARDE during Ar/Cl₂ plasma etching of Si, and, in particular, the role which neutral transport plays in this process. Parametric studies were performed varying neutral-to-ion flux ratios, surface recombination rates of atomic Cl, and neutral and ion angular distributions to determine their influence on neutral transport of Cl to the etch front and ARDE. It was found that each parameter has a significant influence on neutral transport to the etch front (with the exception of the ion angular distribution). Methods for increasing neutral flux (for a given set of ion fluxes) to the etch front were found to push the system toward a neutral saturated, ion starved regime which alleviates ARDE for some range of AR. Increased neutral flux is also correlated with more tapered features, which tend to exhibit more significant ARDE. This coupling of neutral transport with feature profiles makes it difficult to alleviate all ARDE in this system. However, it is possible to optimize parameters in such a way to postpone the onset of ARDE to fairly large AR (>8). © 2017 American Vacuum Society. [<http://dx.doi.org/10.1116/1.4973953>]

I. INTRODUCTION

As feature sizes in microelectronics devices continue to decrease with each technology node, the constraints placed on plasma etching processes become increasingly more stringent.¹ Nonidealities in plasma etching processes, such as line edge roughening,² critical dimension (CD) loss as in Si-recess during gate etching,³ and aspect ratio dependent etching (ARDE),⁴ continue to challenge process development. (Aspect ratio is generally defined as feature height divided by its width.) The transition to three-dimensional (3D) device geometries, such as fin field effect transistors (FinFETs), has exacerbated or complicated the remediation of many of these nonidealities. Of particular interest to etching 3D features is ARDE and the role that neutral transport, which is particularly sensitive to geometry, plays in this process. The sources of, and remedies for, ARDE are significant to several plasma etching processes, and remain a field of active research.^{1,4,5}

Any etching process that relies on fluxes of reactive neutral species that arrive at the wafer with isotropic angular distributions will be subject to the effects of neutral conductance in the transport through the feature of these species from the bulk plasma to the etch front.⁶ Ion fluxes are less sensitive to conductance during their transport through the feature since their angular distributions are usually anisotropic. Due to the pressures and feature length scales typically involved in plasma semiconductor processing, transport within the feature is in the molecular flow regime, meaning that the mean free path between gas phase collisions greatly exceeds the feature size.⁷ In the molecular flow regime, low energy neutral species travel ballistically from surface to surface inside the feature, while typically reflecting (or being re-emitted after adsorption) from the surface with a Lambertian cosine angular distribution.⁸ This process has been studied in the context of vacuum gas transport since early in the development of fluid mechanics,⁹ and has also come to be understood as a major contributing factor to ARDE.⁶

Analytical models incorporating neutral transport^{6,10} and computer simulations^{11–15} have been used to investigate ARDE during plasma etching with different assumptions and levels of detail. While all robust numerical models of plasma

^{a)}Electronic mail: chuard@umich.edu

^{b)}Electronic mail: Yiting.Zhang@lamresearch.com

^{c)}Electronic mail: Saravanapriyan.Sriraman@lamresearch.com

^{d)}Electronic mail: Alex.Paterson@lamresearch.com

^{e)}Author to whom correspondence should be addressed; electronic mail: mjkush@umich.edu

etching of features incorporate the effects of neutral transport, the consequences of neutral conductance are sometimes difficult to discern due to the complexity of the model. Analytical models, on the other hand, can focus more directly on the topic of conductance and neutral transport, but then require simpler representations of the actual etch process. Coburn and Winters, for example, determined that if the etch front consumes incident radicals with a reactive sticking coefficient, S_n , well known vacuum conductance concepts can be used to provide insights to ARDE. They proposed that the ratio of neutral flux arriving at the etch front, Γ_f , compared to the incoming flux from the bulk plasma, Γ_{in} , could be approximated as⁶

$$\frac{\Gamma_f}{\Gamma_{in}} = \frac{K}{K + S_n - KS_n}, \quad (1)$$

where K is the aspect ratio (AR) dependent probability that a randomly directed neutral particle incident on the feature opening will reach the etch front. The parameter K is analogous to Clausing's transmission probability for vacuum systems if the etch front is likened to an opening to a second chamber with zero pressure.¹⁶ The value of K can be calculated analytically for simple shapes (e.g., circular via or two-dimensional trench), or numerically for more complicated shapes. As K decreases with increasing AR, this model predicts a reduction of neutral flux to the etch front, which results in an aspect ratio dependent etch rate. The assumptions required for this expression to be valid are that the side walls do not consume neutrals, and that the reactive sticking coefficient on the etch front, S_n , is constant in time and aspect ratio.

Gottscho *et al.* expanded on the model proposed by Coburn and Winters by introducing the concept of neutral-ion synergy.¹⁰ The basic premise of this model is that S_n is not constant, but rather simultaneously depends on the neutral and ion fluxes at the etch front. In this model, each surface site can only be passivated once, and will then require an ion impact event before the underlying site can accept a new passivating radical. Therefore, high neutral fluxes will progressively produce smaller values of S_n since the available sites may already be occupied by reaction with earlier fluxes. Neutral starved regimes (that is, a low neutral radical flux relative to the ion flux) will have larger values of S_n since there is higher likelihood that sites will be empty. Since the neutral flux reaching the etch front depends on AR, then S_n also depends on AR. Gottscho *et al.* developed analytical expressions for two extreme cases—perfectly diffusive walls (molecular flow) and perfectly absorbing walls (neutral shadowing). Most actual etching processes fall between these two extremes. The model has provided valuable insights for understanding the implications of the neutral-ion synergy and has been used to fit to experimental studies.¹⁷

There are at least two complicating factors when applying analytical models of neutral transport to predicting etch properties for even basic features—neutral consumption by the side walls and varying conductance with profile evolution.

Neutral species can be consumed on the side walls through several processes, including recombination of radicals on the surface to form nonreactive molecules¹⁸ and passivation of exposed silicon sites where off-axis ions have eroded the passivation layer. In addition to changing with aspect ratio, neutral conductance can also significantly change with the shape of the profile. For instance, a tapered feature will have a different conductance than a feature with parallel sides. This issue is further complicated by a profile transitioning from a flat bottomed cylinder or a trench with parallel sides, to a tapered profile as a function of aspect ratio. These changes in profile also have significant effects on the area of the feature that receives high energy particles (ions and hot neutrals following ion neutralization on side walls) which then defines the etch front. These dependencies can lead to significant changes in the effective value of S_n , again impacting the transport of neutral radicals.

When etching simple geometries, such as infinite trenches or circular vias, it is straightforward to establish an aspect ratio—usually height divided by width. This AR can then function as a scaling parameter to describe neutral transport. The ability to so simply specify an AR does not necessarily translate to 3D structures. Since the molecular flow of neutral species through a 3D feature takes place through many adsorption and re-emission events which sample different portions of the 3D feature, it is difficult to *a priori* estimate the conductance between the bulk plasma and any given point on the profile. These issues complicate the extrapolation of our understanding of conductance effects on etching from 1D (e.g., circular vias) or 2D (e.g., infinite trenches) structures to 3D features. The use of numerical models is necessary to accurately evaluate the scaling of neutral transport in features with difficult to define aspect ratios.

To investigate the role of neutral transport on ARDE, and particularly in 3D etching processes, we have used a 3D Monte Carlo simulation. A feature which resembles the shallow trench isolation etch that defines the silicon fins in a FinFET fabrication process has been used for this study. The model system is an inductively coupled plasma (ICP) sustained in an Ar/Cl₂ mixture etching silicon. Several experimental parameters such as the incoming neutral to ion flux ratio and recombination probability of radical Cl atoms on the side walls were varied to determine their effect on ARDE when simultaneously etching several features having different CD. In order to gain additional insights to the causes of ARDE for these conditions, the etch depth dependent fluxes of neutrals and ions to the etch front in a 2D trench were also investigated. We found that for the conditions investigated in this paper, the dominant cause of ARDE is the depletion of neutral species reaching the etch front relative to ions as the AR increases due to neutral transport issues. We also found that increasing the neutral flux reaching the etch front relative to the ion flux can alleviate ARDE for small to moderate AR (<8), but at the expense of producing more tapered features and sometimes increasing ARDE at larger AR.

The methods used in this investigation are described in Sec. II, including a discussion of the reactor scale model,

feature scale model, etch mechanism, and computational metrics used in this study. The scaling of ARDE as a function of the ratio of neutral-to-ion fluxes, recombination of chlorine radicals, neutral angular distributions, ion angular distributions, and width of the feature are discussed in Sec. III. A summary of the results and our remarks are given in Sec. IV.

II. DESCRIPTION OF THE MODEL

For this study, a hybrid simulation technique was used to resolve the various length and time scales. The hybrid plasma equipment model (HPEM) was used to simulate reactor scale plasma properties, and to predict fluxes and angle and energy distributions of ions and neutrals (IEAD and NEAD, respectively) onto surfaces.¹⁹ The Monte Carlo feature profile model (MCFPM) was used to predict etch profile evolution based on the simulated plasma properties. The HPEM has been previously described and will only be briefly discussed here.^{19,20} The mechanics of the 3D MCFPM has also been previously described,²¹ but the chlorine/silicon surface reaction mechanism used for this study has been expanded and will be presented in detail.

A. Reactor scale

The HPEM uses an iterative approach to solve for a quasi-steady-state of the reactor scale properties of the ICP using three main modules. Electromagnetic fields and electrostatic fields from the electromagnetics module and fluid-kinetics module (FKM), respectively, are used to obtain electron impact source functions and transport coefficients in the electron energy transport module. This procedure involves kinetically solving for the electron energy distributions using a Monte Carlo simulation. The results are then used by the FKM to solve continuity, momentum, and energy equations for neutral and charged species. The FKM is also responsible for solving Poisson's equation for the time varying electrostatic potential based on the position dependent charge densities in the volume and on surfaces. The results from the FKM are then used by other modules, and integrated in a time-slicing manner to achieve a time resolved solution. Modules are iterated until cycle-averaged quantities have reached a quasisteady state.

The plasma chemistry Monte Carlo module (PCMCM) of the HPEM uses electron impact source functions along with time resolved electrostatic and electromagnetic fields generated elsewhere in the HPEM to calculate ion and neutral energy and angular distributions incident onto surfaces in contact with the plasma. By generating pseudoparticles based on the electron impact source functions, and using the same reaction mechanism as the FKM to represent collisional processes, the PCMCM tracks particle trajectories using standard Monte Carlo techniques until they interact with surfaces. Once particles strike surfaces their energies and angles (relative to the local surface normal) are binned into the IEAD statistics (and analogous distributions for neutrals, NEAD).

B. Feature scale

The IEADs, NEADs, and fluxes generated by the HPEM are then used by the MCFPM to predict the evolution of etch profiles. Pseudoparticles are randomly chosen from the IEADs and NEADs and launched at a three-dimensional mesh of cubic computational cells, each of which is associated with a single material. Each cell has a volume, V , and material atom density, ρ , resulting in $N = V \times \rho$ atoms per cell. Each pseudoparticle reacts stoichiometrically with one single material cell, and therefore represents N atoms of incoming flux. (Although pseudoparticles can be subdivided into a fraction of a cell, a 1-to-1 ratio was used here.) The actual flux (particles/cm²s) arriving at the surface is calculated by the HPEM, implying that each particle launched toward the surface also represents an increment of time.

The trajectories of the incoming pseudoparticles are advanced in three-dimensions through continuous space until they impact a solid mesh cell. When a pseudoparticle strikes a solid surface, a reaction is chosen from a user defined reaction mechanism. This mechanism can include reactions with both energy and angular dependencies. Based on this reaction mechanism, particle collisions can result in a reflection of the incoming particle without changing the material cell properties, etching of the material cell leaving an empty gas cell, altering the material property of the solid cell, or depositing the incoming pseudoparticle on the surface. After a particle collides with a surface, any resulting particles emitted into the gas phase—including etch products and/or the original particle—are tracked in a similar manner as the initially launched particle until the next collision with a surface. This process is repeated for each particle until that particle (and the gas phase particles it generates) is removed by reacting with a surface, or the particle leaves the computational domain. The simulation proceeds until the desired number of incoming particles are launched and leave the computational domain, or (analogously) a final time is reached.

In order to accurately predict ion and neutral trajectories after collisions with the solid surface, as well as the probability of angularly dependent reactions, the surface normal is calculated at the location of each collision. All locations within a user defined volume ($9 \times 9 \times 9$ nm in this study) of the collision are searched to find a selection of appropriate surface sites (i.e., solid cells with one or more surfaces exposed to the plasma). A Jacobi eigenvalue technique is then used to perform a least-square fit of a plane to these points. The normal vector of this plane facing into the plasma is used as the normal vector of the mesh at the point of collision. Reflections from the surface can contain both specular and thermal components. The specular reflection angle is computed with respect to the surface normal. The direction of the thermal component of velocity is randomly chosen from a cosine Lambertian distribution around the surface normal.

Ions are assumed to be neutralized when striking a surface, and—in the absence of an electric field—are not distinguished from the hot-neutrals which result from reflections of ions from the surface.²² For simplicity, we use the term

ion to denote a hot, nonthermal, particle—the initial ion before striking a surface or the hot-neutral after striking a surface. In this study, ions reflect from surface collisions at a specular angle with an energy 85% of the incoming energy at grazing incidence, decreasing to thermal energy for angles of incidence smaller than 60° from the normal. Ions whose energy drops below 1 eV by energy lost through reflections are converted to their thermal neutral counterparts, and are then indistinguishable from the incoming neutral flux of that species.

Neutral transport through high-aspect ratio features has a strong influence on ARDE. To validate the neutral transport aspects of our model, test problems were simulated and compared to results of analytical models by Clausing¹⁶ of neutral transport in the molecular flow regime. The transmission of neutral fluxes through a circular tube was computed with the MCFPM, and transmission probabilities were derived as function of AR. (Transmission probability is the ratio of the number of neutral particles which emerged from the far end of the tube divided by the number of particles entering the tube.) The computed transmission probabilities agreed with theory with an error of <6% over the range of AR studied. The error was directly related to the discretization of a circular tube by a rectilinear mesh and not due to any issue with the neutral transport model itself.

Validation of the MCFPM was recently discussed by comparing simulated profiles with experiments for features etched in a He/Cl₂ plasma.²¹ The details of the etching mechanism in that study differ from the mechanism used here. However, the basic processes are the same in both mechanisms.

C. Etch mechanism

The etching of silicon by Ar/Cl₂ plasmas proceeds by first passivating the surface with chlorine. The process begins with a reaction of a Cl radical with the bare silicon surface to form SiCl_(s). Subsequent reactions with chlorine further chlorinate the SiCl_(s) surface to form SiCl_{x(s)}, where $x < 4$.^{23–25} The surface reaction mechanism used in this investigation is outlined in Table I. In our model, this process is represented by having a series of materials which represent different chlorination levels: Si_(s), SiCl_(s), SiCl_{2(s)}, and SiCl_{3(s)}. Each of these materials with $x < 3$ can undergo additional chlorination reactions, with successively lower probabilities, to increase the chlorination level to SiCl_{x+1(s)}. The probabilities of passivation are 99%, 40%, and 30% for $x = 0, 1, \text{ and } 2$. As these materials are applied to entire computational cells, which can represent several atoms, they are not meant to exactly represent the chlorination state of every silicon atom in the cell, but rather they represent an increasing average surface chlorination level. At pressures above a few mTorr, this chlorination process is carried out mostly by Cl radicals; however, Cl₂⁺ and Cl⁺ species are also capable of chlorinating surface sites in this mechanism. Thermal etching is included, with a small probability, by the chlorination of a SiCl_{3(s)} site by a Cl radical to form volatile SiCl₄—that is, the surface site is converted to a gas phase SiCl₄

TABLE I. Surface reaction mechanism.

Reaction	Probability ^a	ϵ_{th} (eV) ^a	p_0 ^a	Angle ^b	Notes
Cl radical reactions					
(1) Si _(s) + Cl → SiCl _(s)	0.99				
(2) SiCl _(s) + Cl → SiCl _{2(s)}	0.40				
(3) SiCl _{2(s)} + Cl → SiCl _{3(s)}	0.30				
(4) SiCl _{2(s)} + Cl → SiCl _(s) + Cl ₂	0.02				
(5) SiCl _{3(s)} + Cl → SiCl ₄	0.0001				
(6) SiCl _{3(s)} + Cl → SiCl _{2(s)} + Cl ₂	0.08				
(7) R _(s) + Cl → R _(s) + Cl	1.00				c
Redeposition					
(8) M _(s) + SiCl _x → M _(s) + SiCl _{x(s)}	0.02				d
Ion reactions					
(9) Si _(s) + Cl ⁺ → Si + Cl [*]		25	0.05	P	e, f
(10) SiCl _(s) + Cl ⁺ → SiCl ₂		35	0.10	P	e
(11) SiCl _(s) + Cl ⁺ → SiCl ₂		10	0.20	C	e
(12) SiCl _{2(s)} + Cl ⁺ → SiCl ₂ + Cl [*]		10	0.50	C	e, f, g
(13) SiCl _{3(s)} + Cl ⁺ → SiCl ₃ + Cl [*]		10	0.50	C	e, f, g
(14) R _(s) + Cl ⁺ → R + Cl [*]		15	0.01	P	c, e, f
(15) Si _(s) + Cl ₂ ⁺ → Si + Cl ₂ [*]		25	0.02	P	e, f
(16) SiCl _(s) + Cl ₂ ⁺ → SiCl ₂ + Cl [*]		10	0.20	C	e, f, g
(17) SiCl _{2(s)} + Cl ₂ ⁺ → SiCl ₂ + Cl ₂ [*]		10	0.25	C	e, f, g
(18) SiCl _{2(s)} + Cl ₂ ⁺ → SiCl ₃ + Cl [*]		10	0.25	C	e, f, g
(19) SiCl _{3(s)} + Cl ₂ ⁺ → SiCl ₃ + Cl ₂ [*]		10	0.25	C	e, f, g
(20) SiCl _{3(s)} + Cl ₂ ⁺ → SiCl ₄ + Cl [*]		10	0.25	C	e, f, g
(21) R _(s) + Cl ₂ ⁺ → R + Cl ₂ [*]		15	0.01	P	c, e, f
(22) Si _(s) + Ar ⁺ → Si + Ar [*]		25	0.05	P	e, f
(23) SiCl _(s) + Ar ⁺ → SiCl + Ar [*]		10	0.20	C	e, f, g
(24) SiCl _{2(s)} + Ar ⁺ → SiCl ₂ + Ar [*]		10	0.50	C	e, f, g
(25) SiCl _{3(s)} + Ar ⁺ → SiCl ₃ + Ar [*]		10	0.50	C	e, f, g
(26) R _(s) + Ar ⁺ → R + Ar [*]		15	0.01	P	c, e, g

^aIf ϵ_{th} and p_0 are blank the reaction has no energy dependency, and the reaction probability is constant.

^bAngular dependence of the reaction. P = physical sputtering, C = chemical sputtering, blank for reactions with no angular dependency.

^cR_(s) is the solid photoresist. The gas phase etch product, R, is assumed to be volatile and does not redeposit on feature surfaces.

^dRedeposition reaction. M_(s) denotes any solid surface. SiCl_x ($x = 1, 2, 3$).

^eEnergy dependent reaction with probability defined by Eq. (2) with $\epsilon_D = 100$ eV. Probability is renormalized as necessary, as described in the text. When probability of reaction is less than unity, remaining probability is allocated to nonreactive reflection (other than neutralization of ions).

^fAsterisk superscript (i.e., Cl^{*}) indicates a hot neutral. Hot neutrals have identical reactions and probabilities as the corresponding ion.

^gA reaction with the same reactants and products is also included, but with physical sputtering angular dependence, $\epsilon_{th} = 35$ eV and $p_0 = p_{0(c)}/2$, where $p_{0(c)}$ is the p_0 of the (listed) chemical sputtering reaction. Reactions (10) and (11) show this relationship explicitly.

particle, which is emitted from the feature leaving behind a vacated surface cell.

The recombination of atomic Cl on surfaces is incorporated into the reaction mechanism as an Eley–Rideal (ER) type reaction. In this reaction, chlorine radicals impinging on SiCl_{x(s)} ($x = 2, 3$) sites can abstract one of the chlorine atoms from the solid surface and return to the gas phase as Cl₂, leaving SiCl_{x-1(s)} on the surface. Reactions (4) and (6) in Table I show the recombination reactions and probabilities as included in the base case. We assumed that SiCl_(s) represents a strongly chemisorbed state which does not allow

recombination abstraction reactions. The reaction probabilities in the basic mechanism (Table I) result in a chlorine recombination coefficient of 0.07 on a steady-state passivated surface. Due to the disordered nature of the amorphized silicon layer resulting from plasma exposure, the recombination coefficient was chosen to be between the measured values for pristine crystalline silicon (<0.01) and polysilicon (≈ 0.14) in a neutral beam experiment.¹⁸ This value is also similar to the recombination coefficient of 0.03 on a plasma exposed silicon oxy-chloride surface, as measured by Khare *et al.* using the spinning wall technique.²⁶ Cunge *et al.* have measured lower recombination coefficients of 0.005–0.007 on the SiOCl surfaces formed in Cl₂/O₂ plasmas.²⁷ Although there is always some likelihood for oxygen contamination from sputtering of alumina or quartz in contact with the plasma, we expect that the proportion of SiOCl sites to be smaller than in a plasma with O₂ as a feedstock gas. While the experimental data can be fit well with a Langmuir-Hinshelwood (LH) model,^{18,26} most of the recombination for our conditions occurs on the fully saturated sidewalls. For these saturated conditions, the ER and LH models are expected to converge.

The chlorinated passivation layer has an increased sputtering yield when compared to the bulk silicon, and enables energetic ions to preferentially remove this mixed layer. The nature of the strong Si–Cl bond is such that, with increasing chlorine coordination, the remaining Si–Si bonds with the underlying lattice weaken, as has been shown experimentally and through the use of first-principles density functional theory.^{23,25,28} This process is represented by using energy dependent sputtering probabilities with larger yields for the more chlorinated surface species. The probability for sputtering a surface site is given as

$$P_{SP}(\varepsilon) = p_0 \left(\frac{\varepsilon - \varepsilon_{th}}{\varepsilon_0 - \varepsilon_{th}} \right)^{1/2}, \quad (2)$$

where ε_{th} is the threshold energy for the process, ε_0 is a reference energy, and p_0 is the probability at the reference energy. Chemical sputtering of all SiCl_{*x*(s)} surface sites have a threshold energy of 10 eV, and values of p_0 which increase with chlorine coordination. For $\varepsilon_0 = 100$ eV, $p_0 = 0.20, 0.50,$ and 0.50 for SiCl_(s), SiCl_{2(s)}, and SiCl_{3(s)}. Direct sputtering of unpassivated silicon sites was included with a threshold energy of 25 eV ($\varepsilon_0 = 100$ eV, $p_0 = 0.05$). In this model, each gas pseudoparticle can only react with a single solid cell, including sputtering reactions. This limitation poses a problem for process conditions where there are high ion energies and high neutral-to-ion flux ratios. For these conditions, experiments show that the etch yield per ion can exceed one.²⁹ Our sputter yield parameters were chosen to best represent experimental trends over a wide range of etching conditions while acknowledging that our etch yields will be low when operating with high ion energies and high neutral-to-ion flux ratios.

In addition to a dependence on ion energy, sputtering reactions also have a dependence on the angle of incidence of the impinging particle with respect to the local surface

normal. This angular dependence for chemically enhanced sputtering involving a passivating species is typically different from that for direct physical sputtering.^{11,30} There is evidence that both physical and chemical sputtering mechanisms can be simultaneously active, with chemical sputtering dominating at low ion energy and physical sputtering becoming more important as ion energy increases.^{15,31,32} Different processes, each with a different threshold energy (ε_{th}) and reaction probability (p_0), are used to represent these two reactions. Physical sputtering reactions have a peak in their probability for angles of incidence around 60°, with reduced probability at normal incidence and zero probability at grazing incidence. These reactions were given higher threshold energies than chemically enhanced processes, and lower etch probabilities for more chlorinated species. Chemically enhanced sputtering reactions have unity probability for normal incidence and angles up to 45°, with a monotonic roll-off above this value to zero probability at grazing incidence.

When the energy and angle dependent reactions for a given gas phase species and surface site have probabilities that sum to less than 1, the remaining probability is assigned to a nonreacting reflection of the incident gas phase particle (which includes a neutralization for ions). For incident particles that have energies lower than any threshold for a surface reaction, this process results in a reflection probability of one. If the energy dependent probability, or sum of multiple energy dependent probabilities, is greater than one, the total is renormalized to unity and the probability of sample reflection goes to zero.

Gas species generated deep in the feature, such as etch or recombination products, must diffuse out of the feature by molecular flow before returning to the bulk plasma. The etch products are typically neutral, often are radicals, and generally have approximately thermal energy. Radical etch products (SiCl_{*x*}, $x < 4$) have a finite probability of redepositing within the feature each time they strike the surface. The sticking coefficients for SiCl on SiOCl coated reactor walls has been measured to be near unity, while SiCl₂ has lower sticking probability of 0.05.²⁷ In our mechanism, a sticking coefficient of 0.02 was chosen for all SiCl_{*x*} ($x < 4$) etch products on all other solid surfaces. While fluxes of SiCl_{*x*} and SiCl_{*x*}⁺ returning to the feature from the bulk plasma have been shown to be important in industrial plasmas^{33,34} their contributions have been neglected here for simplicity.

D. Computational metrics

To quantify the role that system parameters may have on ARDE several metrics were developed. These metrics will be discussed in this section.

1. Etch rate

The instantaneous etch rate was calculated by measuring the average height of the solid surface in a 7×7 nm window at the center of the feature for equally spaced time steps. The first order derivative of the height with respect to time provides the etch rate. Due to the stochastic nature of the simulation and the finite resolution of the mesh, this derivative

can often be noisy. To obtain better statistics, averaging and error analysis were performed over multiple simulations. The resolution of the mesh at times approaches atomic dimensions. In those cases, the stochastic nature of the results reflects the natural statistical variation of the process.

The fundamental metric of ARDE is etch rate as a function of aspect ratio. However the aspect ratio (calculated at each time step) is not evenly spaced in time since the etch rate is not necessarily constant. Averaging was performed by fitting a third order spline to etch rate (measured at each time step) as a function of aspect ratio (calculated at each time step) for each data set. The average and standard deviation of the resulting collection of splines was then taken on a grid evenly spaced in aspect ratio. Unless otherwise noted, instantaneous etch rates were normalized to the etch rate of the base case in the *open field* (obtained from the simulation of an unpatterned wafer).

2. Fluxes at the etch front

Fluxes and energies of particles incident onto the etch front window were measured by counting the number, angle of incidence, and energy of pseudoparticles that impact the same 7×7 nm window used for the calculation of etch rate. Neutral species fluxes were calculated as simple rates of incidence. The number of impacts of each pseudoparticle representing a given species arriving at the etch front window was scaled by the weight of a single pseudoparticle (the number of atoms or molecules each pseudoparticle represents) and divided by the surface area of the cell collecting the particle. To be representative of neutral transport, the chlorine flux is based only on the radical Cl species. The chlorine flux measurement does not directly include fluxes of Cl^+ , or Cl_2^+ , but does include the flux of Cl which is generated within the feature as a result of neutralization and thermalization of Cl^+ or dissociation of Cl_2^+ after reactions with the surface. Energetic species are also scaled by the dot product of the particle's velocity unit vector and the surface normal at the site of incidence. The power density is then calculated as the sum of the fluxes of each energetic particle species multiplied by the average energy of that species at the etch front. All results are then averaged from multiple simulations using the spline fitting technique described for the measurement of etch rate.

III. SCALING OF ARDE

The reactor used in this study is an inductively coupled plasma etch chamber. The reactor geometry is 22.5 cm in diameter and is shown in Fig. 1(a). For all simulations, 150 W of power was delivered to the plasma through a three-turn antenna (powered at 10 MHz) located above a quartz window 10 cm from the wafer surface. The wafer (15 cm diameter) was mounted on a metallic chuck with an applied radio frequency bias having an amplitude of 150 V at 10 MHz. The gas mixture was $\text{Ar}/\text{Cl}_2 = 80/20$ with an incoming flowrate of 200 sccm. The chamber was maintained at 20 mTorr pressure by adjusting the outflow pumping rate, as in a feedback controlled gate valve. The resulting maximum positive ion

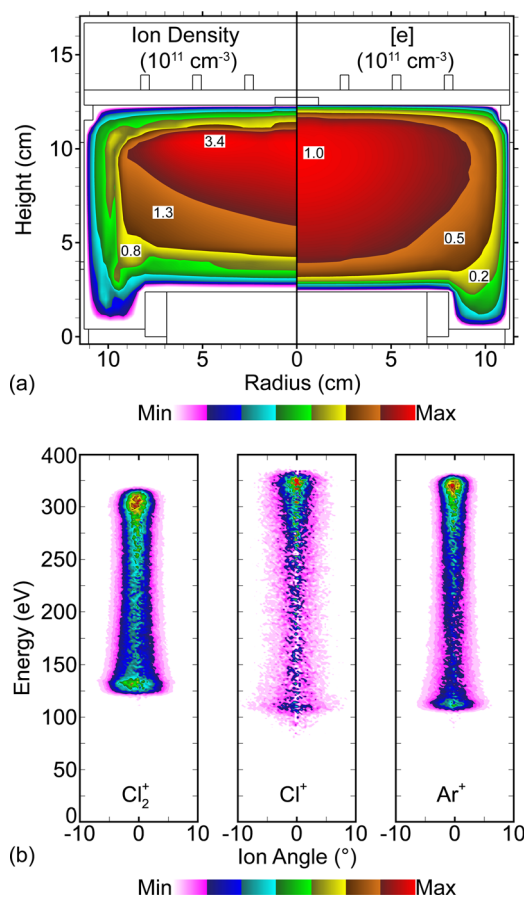


Fig. 1. (Color online) Reactor and plasma properties. (a) Reactor geometry with (left) total positive ion density and (right) electron density, shown on a log scale with a range of two decades. (b) Probability density of ions reaching the wafer surface as a function of ion energy and incident angle (IEAD), shown on a linear scale.

density, shown in Fig. 1(a), is $3.4 \times 10^{11} \text{ cm}^{-3}$ and the electron density is $1 \times 10^{11} \text{ cm}^{-3}$, indicating an electronegativity of about 2.5. The resulting dc bias on the substrate is -113 V , which generates IEADs to the substrate that are bimodal with peaks around 125 and 325 eV and average angular distributions of $\pm 2.22^\circ$ (half-width-half-max), as shown in Fig. 1(b). These IEADs were used for all cases discussed here, unless specified otherwise. The fluxes to the substrate used in the simulations (unless specified otherwise) are $\text{Cl} = 2.2 \times 10^{17} \text{ cm}^{-2} \text{ s}^{-1}$, $\text{Cl}^+ = 1.0 \times 10^{16} \text{ cm}^{-2} \text{ s}^{-1}$, $\text{Cl}_2^+ = 8.3 \times 10^{15} \text{ cm}^{-2} \text{ s}^{-1}$, and $\text{Ar}^+ = 6.1 \times 10^{14} \text{ cm}^{-2} \text{ s}^{-1}$, which were adjusted from the HPEM results to give a smaller neutral to ion ratio reaching the wafer.

With the goal of understanding the consequences of neutral transport on ARDE when etching 3D features having different effective aspect ratios, a model geometry was used that is similar to the shallow trench isolation etch used to define the fins in a FinFET process. The feature consists of 30 nm wide fins with a pitch of 80 nm and a finite length of 400 nm, as shown in Fig. 2. The fins are arranged in a subarray of three fins separated from other subarrays by a 200 nm gap in the transverse (X) direction, and 100 nm in the longitudinal (Y) direction. The actual simulation domain consisted of one subarray of three fins, with periodic boundary

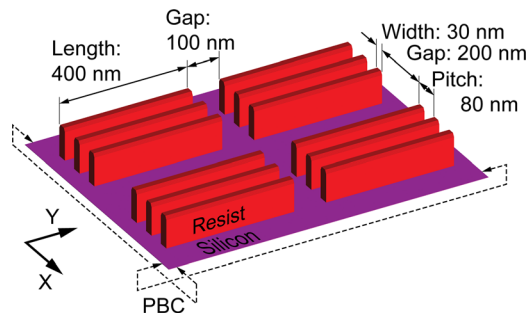


FIG. 2. (Color online) Mask pattern used for etching FinFET geometries. The simulation domain includes one subarray of three fins with periodic boundary conditions.

conditions, having the effect of simulating a larger array of identical structures. The region having a lower aspect ratio in the area between the subarrays is referred to as the *open field*.

The resulting 3D etch profile is shown in Fig. 3. In the 50 nm wide trenches between the fins, the total etch depth is significantly smaller than in the open field between the subarrays, as shown in Fig. 3(b). These trends indicate that there is an ARDE effect in the base etching mechanism. In addition to lower etch rates in the high AR trenches, etch depth is also a function of position along the finite trench, visible in Fig. 3(a) and discussed below, resulting in a significantly deeper trench at the ends of the finite length fins than in the middle of the feature.

The origins of the differences in total etch depth between the 50 nm wide trenches and the open field in the transverse X-section, and along the longitudinal length of the trenches (Y-direction), lie with the relative values of power density and neutral flux to these surfaces, as shown in Fig. 4. The power density delivered to the horizontal surfaces by energetic ions, shown in Fig. 4(a), is nearly uniform along the length of the trenches, as well as in the open field. This lack of sensitivity to AR results from the ion angular distribution being sufficiently anisotropic (that is, a narrow angular distribution about the wafer surface normal), and the side wall scattering being sufficiently specular, that the view-angle to the plasma of sites on all horizontal surfaces subtends the majority of the ion fluxes.

On the other hand, the flux of chlorine radicals incident onto surfaces, shown in Fig. 4(b), decreases from the top of the feature to the bottom, as well as decreasing longitudinally from the open field at the ends of the trench to the center of the trench. This strong dependence of neutral radical fluxes on the vertical position within the trench implies an aspect ratio dependence. This dependence on AR results from the flux of chlorine radicals incident onto the etch feature being essentially isotropic in the direction toward the wafer, and relying on diffusive neutral transport to reach the etch front. The relative insensitivity of power density to the etch front as a function of AR, compared to the strong dependence of neutral flux, indicates that neutral transport likely dominates the ARDE process for this mechanism. The longitudinal dependence of the chlorine flux and etch rate along the trench indicates a significant 3D component to

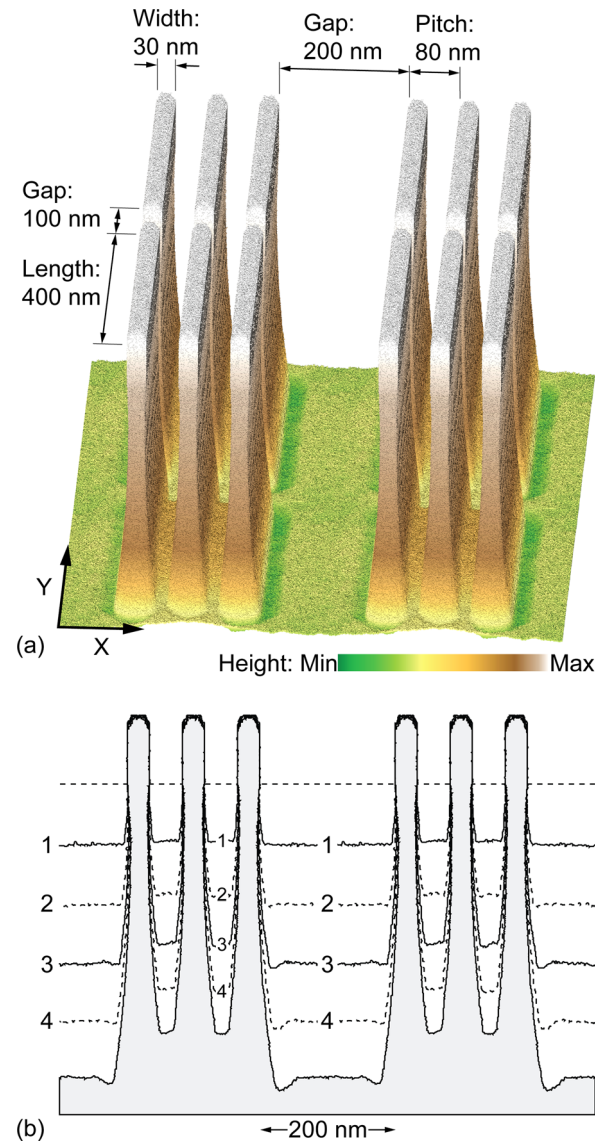


FIG. 3. (Color online) Etched profiles for the FinFET geometry. (a) Perspective view of the height of the feature, showing the variation of etch depth in the longitudinal Y-direction between fins. The difference between the total etch depth between the fins and the open field is also visible. (b) Slice through the fins in the X-direction, taken at the center of the fin length. Each line is separated by a constant time interval.

neutral transport. There is an *effective aspect ratio* which depends on etch depth and proximity to the open field at the ends of the trench. The effective aspect ratio is larger in the center of the trench and smaller near the ends.

The lower effective aspect ratio near the ends of the trenches is partly due to an increase in the view-angle to the plasma at the ends of the trench relative to the view-angle to the plasma in the center of the trench. This larger view-angle intercepts more of the isotropic flux of Cl atoms than at the center of the trench. There is also a contribution of diffusively scattered Cl atoms from the surface of the open field adjacent to the trench. These diffusively reflected Cl atoms enter the trench from the end, often near the bottom of the feature. This proximity to the etch front, combined with the stochastic nature of the molecular flow of neutral species in

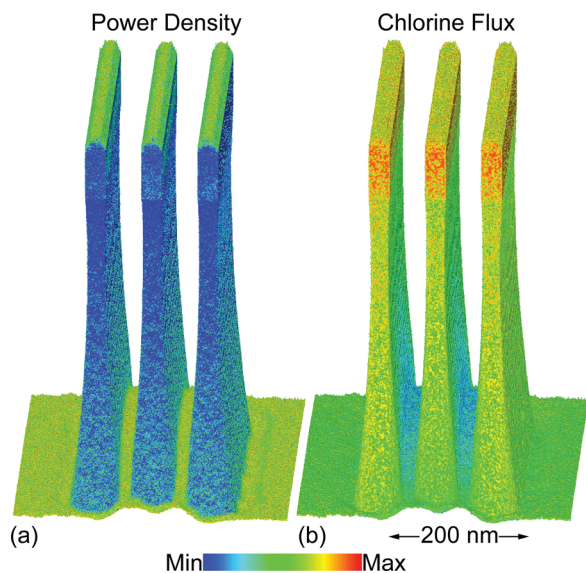


FIG. 4. (Color online) Spatially resolved fluxes to the surface of the etch profile. (a) Power density delivered by ions and (b) chlorine radical flux.

the feature, results in these Cl atoms having a much larger probability of reaching the etch front compared to Cl atoms entering the feature from the top. These conditions can be interpreted as a reduction in the effective aspect ratio at the longitudinal ends of the finite length fins due to the proximity to the open field.

Etching of the same FinFET layout having different fin lengths—200, 400, and 600 nm—was simulated to estimate the range of feature dimensions susceptible to these 3D transport issues. The results are shown in Fig. 5. At the center of the 600 nm fin, there is a region of nearly uniform etch depth with an aspect ratio of ≈ 10 , based on the width of the trench and etch depth of the feature at that point. At the ends of the fin, the trench is the nearly the same depth as the open field (ignoring microtrenching), which has an aspect ratio of ≈ 3.5 . There is a 200 nm long region, starting at the ends of the 600 nm fin and progressing toward the center, where the etch front transitions from the etch depth of the open field to the shallower etch depth at the center of the fin. This region of varying etch depth is sensitive to the 3D transport of neutral radicals entering from the ends of the fin in addition to those radicals entering from the top of the feature. At shallower total etch depths (not shown), there are smaller differences in etch depth between the center of the trench and the open field. However, the length along the trench that is sensitive to 3D transport is approximately the same.

The etch depth for the 200 nm fin is a function of position along its entire length, indicating that 3D transport of Cl radicals is important throughout the feature. The etch depth for the 600 nm fin is constant for the center half of the trench, a region that is not overly sensitive to 3D transport. The 400 nm fin lies somewhere between these two extremes, having a short length in the center of the trench which is not sensitive to 3D transport of Cl radicals. These trends indicate that it may be useful to consider an effective *horizontal aspect ratio*. This metric is the ratio of horizontal distance

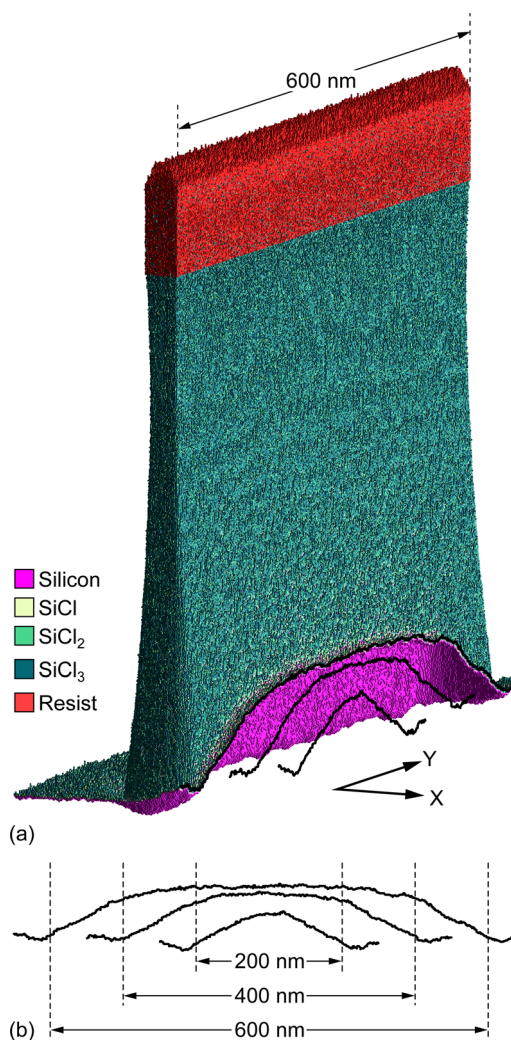


FIG. 5. (Color online) Longitudinal slice (Y-direction) through the center of the trench in the 3D FinFET, showing the etch front (solid lines) for three fin lengths: 200, 400 and 600 nm. (a) Perspective view of the feature showing surface material. (b) Height at the bottom of the trench in the longitudinal (Y-direction) for different fin lengths. (The nominal fin lengths are shown as dotted lines for reference.)

from a site to the open field divided by the width of the feature (50 nm in this case). This feature and reaction mechanism has a local etch rate which depends on horizontal aspect ratio up to ≈ 4 , above which 3D transport issues no longer dominate.

To investigate the effects of ARDE without the complications of 3D transport resulting from end effects, simulations were performed of etching effectively 2D trenches having different widths—33, 50, and 67 nm. These profiles were modeled in 3D while using periodic boundary conditions at the open ends of the features, which has the result of making the trench appear to be infinitely long. The three features were etched during the same simulation to minimize the stochastic effects that might result from separate simulations. The resulting etch profiles, shown in Fig. 6(a), have a dependence of final etch depth on feature size, with smaller features etching slower than larger ones. (The lines in each of the features show intermediate profiles at the same times.) In the time required to etch the 67 nm (left-most) trench to a

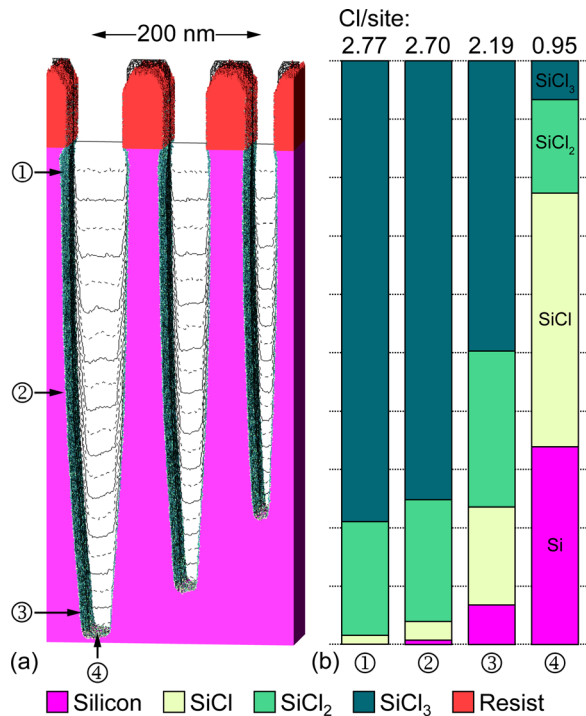


FIG. 6. (Color online) Etch properties for trenches. (a) Simultaneously etched profiles showing ARDE for three trenches having different widths, showing different solid materials. Black lines represent slices through the center of the trench at different times, taken at constant time intervals. (b) Normalized density of surface species at different locations along the 67 nm profile. The etch front measurement is taken on the horizontal surface being bombarded by ions. Side high, mid and low measurements are taken from the side wall just below the resist, halfway down the profile and just above the etch-front. All chlorination measurements were taken at the final time step.

depth of 600 nm, the 50 nm (center) trench has only etched to a depth of 540 nm and the 33 nm (right-most) trench has only reached a depth of 450 nm. The differences in etch depth increase with increasing etch time.

The yield for chemically enhanced sputtering in our mechanism increases for increasingly chlorinated silicon sites. The chlorination state of the site is therefore an important metric when evaluating etch results. The normalized surface concentrations of SiCl_x(s) at four points along the profile of the 67 nm trench are shown in Fig. 6(b). The upper portion of the trench under the resist is heavily chlorinated, with an average of 2.8 chlorine atoms per silicon surface site. The concentrations at the middle of the side wall (labeled 2 in Fig. 6) are similar to that higher in the trench (labeled 1). The concentrations 10 nm above the bottom of the features (labeled 3) have significantly more SiCl and bare silicon sites, with a proportional decrease in the SiCl₃ coverage, having an average of 2.2 Cl atoms per surface site. This lowering of the chlorination is dominantly due to primary ions impacting the mildly sloped side walls and etching these sites. Primary ion impacts with the side walls, even at this side wall slope, are at grazing angles and mostly reflect off the surface becoming hot neutrals. Nonetheless, a significant number of SiCl₃ sites are being etched at this location in the profile. These heavily chlorinated Si sites are

consistent with XPS measurements of Petit-Etienne *et al.* who observed that nearly half of the SiCl_x sites in similar Cl₂ plasmas are composed of SiCl₃.³⁵

The chlorination density of the horizontal etch front at the bottom of the feature provides insights to the origins of ARDE. Ion starved processes (etch rate limited by the flux of ions) have a high chlorination density at the etch front. Neutral starved processes (etch rate limited by the flux of Cl atoms) have lower chlorination and bare Si sites. At the bottom of the 67 nm wide trench with an etch depth corresponding to an aspect ratio of 3.25, the surface sites are 14% bare Si, 29% SiCl, 26% SiCl₂, and 30% SiCl₃, resulting in an average of ≈ 1.7 chlorine atoms per surface site. After etching to an aspect ratio of 10.4 the surface sites are 34% bare Si, 43% SiCl, 16% SiCl₂, and 7% SiCl₃, with ≈ 0.95 chlorine atoms per surface site, as shown in Fig. 6(b). The changing composition of chlorination as a function of depth and aspect ratio contributes to ARDE.

The surface chlorination as a function of etch depth is shown in Fig. 7 for each of the three feature widths. Each feature has two distinct regimes to the surface chlorination. The surface chlorination decreases as etch depth increases with a slope inversely proportional to feature width for small etch depths. At larger etch depths, the surface chlorination is nearly independent of etch depth, though lower for narrower features. The etch depth at which the chlorination becomes constant depends on the width of the feature, shallower depths for narrower features. However, the depth corresponds to an AR of 7 for each feature. The fluxes of the initially isotropic Cl atoms that reach the bottom of the feature decrease with etch depth. The fact that the chlorination eventually becomes independent of etch depth for all feature widths implies that chlorination is not solely a function of the transport of radicals from the bulk plasma through the trench. At these etch depths, a significant fraction of the Cl atoms producing surface passivation is delivered by ions having anisotropic trajectories. These Cl atoms are delivered either directly to the surface or following neutralizing, grazing collisions on the side walls. This decrease in chlorine passivation on the surface of the etch front with increasing

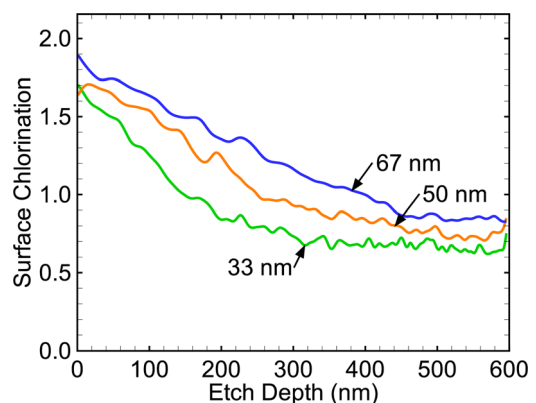


FIG. 7. (Color online) Average surface chlorination (Cl atoms per silicon site) of the etch front as a function of etch depth for trenches having widths of 33, 50, and 67 nm.

aspect ratio significantly affects the etch rate and directly contributes to ARDE.

The consequences of transport of energetic particles (ions and hot neutrals) also play a role in the profile evolution and ARDE. Two such consequences are microtrenching and ion funneling. Microtrenches are the small features of localized deeper etching at the foot of vertical, or nearly vertical, side walls. These microtrenches occur at the base of the side walls adjacent to the open field of our 3D test structure, as shown in Fig. 3. Microtrenches are the result of the specular reflection of grazing incidence ions (or hot neutrals) from the side walls, effectively increasing the power density delivered to the corners of the trench.^{36,37} In the 67 nm trench shown in Fig. 6(a), and to a lesser extent the 50 nm trench, microtrenches appear at aspect ratios of about 3–6. As the etch progresses, the slight taper of the profile begins to draw the microtrenches together until they merge. After the microtrenches have merged, ions reflected by grazing collisions with the tapered side walls impinge on the entire etch-front as opposed to the isolated corners. When combined with the primary anisotropic ions from the plasma, the additional contributions of the reflected ions can increase the etch rate in the feature as a whole. This effect will be referred to here as *ion funneling*. After the onset of ion funneling, the etch continues with a relatively flat etch front. The width of the etch front after the microtrenches have merged remains fairly constant and is proportional to the CD of the respective feature, which is the width of the photoresist opening in these cases.

A. Neutral to ion flux ratios

If neutral starvation in the areas of a 3D feature having high AR is a dominant cause of ARDE, then increasing the ratio of neutral fluxes to ion fluxes is potentially a means to reduce ARDE. While these two fluxes are usually linked through the properties of the plasma producing the fluxes, artificially adjusting the fluxes provides insights to the causes of ARDE. In this regard, the magnitude of the incident ion flux (Γ_i) was varied while keeping the shape of the IEAD and the incident neutral flux (Γ_n) constant. Simulated profiles for etching the FinFET structure with $\Gamma_n/\Gamma_i = 5, 10,$ and 20 (the base case has $\Gamma_n/\Gamma_i = 11.6$, for reference) are shown in Fig. 8(a). The etch rate in the open field is highly dependent on the Γ_n/Γ_i ratio, which complicates making comparisons at equal etch times. For example, the initial etch rates for the first 6 s in the 50 nm trench are 1.66, 1.04, 0.58, and 0.41 times that of the base case for $\Gamma_n/\Gamma_i = 5, 10, 20,$ and 30 . This trend indicates that the etch rate in the open field is dominantly ion starved—there is sufficient Cl radical flux to nearly fully passivate sites and so the etch rate increases nearly linearly with increasing ion flux. As discussed previously, for a given ion flux, ARDE depends on the arrival of neutral flux at the etch site. As a result, ARDE behaves as though the process is neutral starved, higher ratios of Γ_n/Γ_i reduce the dependence of etch rate on etch depth. Lower or higher absolute etch rates do not necessarily correspond to more or less sensitivity to ARDE.

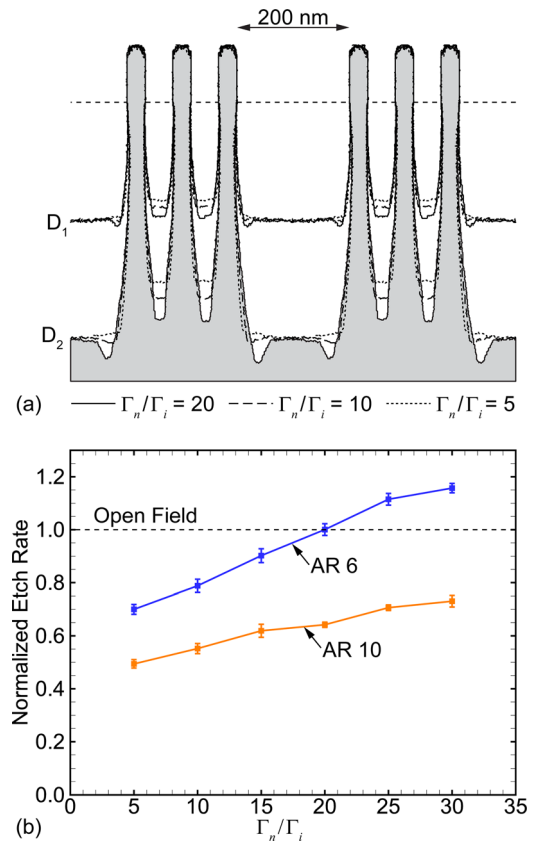


FIG. 8. (Color online) Etch properties for different values of Γ_n/Γ_i . (a) Two dimensional slice through FinFET profile for several incoming neutral to ion flux ratios. The lines labeled D_1 and D_2 represent equal etch depths, and are taken at different etch times due to the different etch rates between cases. The slice is taken through the center of the length of the fin. (b) Normalized etch rates as a function of Γ_n/Γ_i for two different AR. Etch rates are normalized to the initial etch rate of each respective Γ_n/Γ_i to enable comparison.

To minimize the consequences of absolute etch rates and so emphasize ARDE, the profiles marked D_1 and D_2 in Fig. 8(a) are shown at equal etch depths in the open field instead of equal etch times. Larger Γ_n/Γ_i results in more tapered features in the trenches, while lower Γ_n/Γ_i (higher ion flux) produces a more ideal, flat bottomed profile. No microtrenching is evident inside the trenches because the widths of the expected microtrenches are commensurate with the width of the feature. However, the tapered side walls indicate that ion funneling may be important. On the other hand, there is microtrenching at the base of the side wall facing the open field, and the degree of microtrenching is sensitive to Γ_n/Γ_i . Larger values of Γ_n/Γ_i produce more microtrenching.

The ratio Γ_n/Γ_i also affects ARDE. As a reference, the etch depth in the open field suffers from little, if any ARDE. At the intermediate level, D_1 , the etch depth in the trenches for $\Gamma_n/\Gamma_i = 20$ is nearly the same as that in the open field, whereas the etch depths for the lower values of Γ_n/Γ_i lag behind the open field. At the deeper level, D_2 , the etch depth for $\Gamma_n/\Gamma_i = 20$ begins to lag behind that of the open field, indicating the onset of ARDE, an effect that is more pronounced with decreasing Γ_n/Γ_i .

The dependence of ARDE on Γ_n/Γ_i also changes with the aspect ratio. Normalized etch rates as a function of Γ_n/Γ_i are

shown in Fig. 8(b) for two values of AR. Note that each Γ_n/Γ_i is normalized to its own initial etch rate. If the results were normalized to a single etch rate in the open field—say, that of the base case—the line labeled “Open Field” would be sloped. The etch rates for each AR are obtained at different times for different values of Γ_n/Γ_i which is due to the difference in absolute etch rates. For AR = 10, the normalized etch rate monotonically increases by 46%, from 0.50 to 0.73, for Γ_n/Γ_i increasing from 5 to 30. At AR = 6 (which corresponds approximately to when ion funneling begins), the dependence of normalized etch rate on Γ_n/Γ_i is stronger. The normalized etch rate increases by 66%, from 0.70 to 1.16 times the etch rate in the open field, for Γ_n/Γ_i increasing from 5 to 30. For $\Gamma_n/\Gamma_i > 20$, the taper of the feature is severe enough that ion funneling increases the etch rate above that of the open field. Etch rates in the trench that are higher than the open field occur, in this model, only over a small range of AR, as discussed below.

To more quantitatively investigate the consequences of Γ_n/Γ_i on ARDE, etching of 2D trenches with a width of 50 nm were simulated for $\Gamma_n/\Gamma_i = 5$ to 30. The resulting profiles are shown in Fig. 9 for $\Gamma_n/\Gamma_i = 5, 10$, and 20. Lower values of Γ_n/Γ_i etch faster for the entire duration of the etch while larger values of Γ_n/Γ_i produce more tapered profiles,

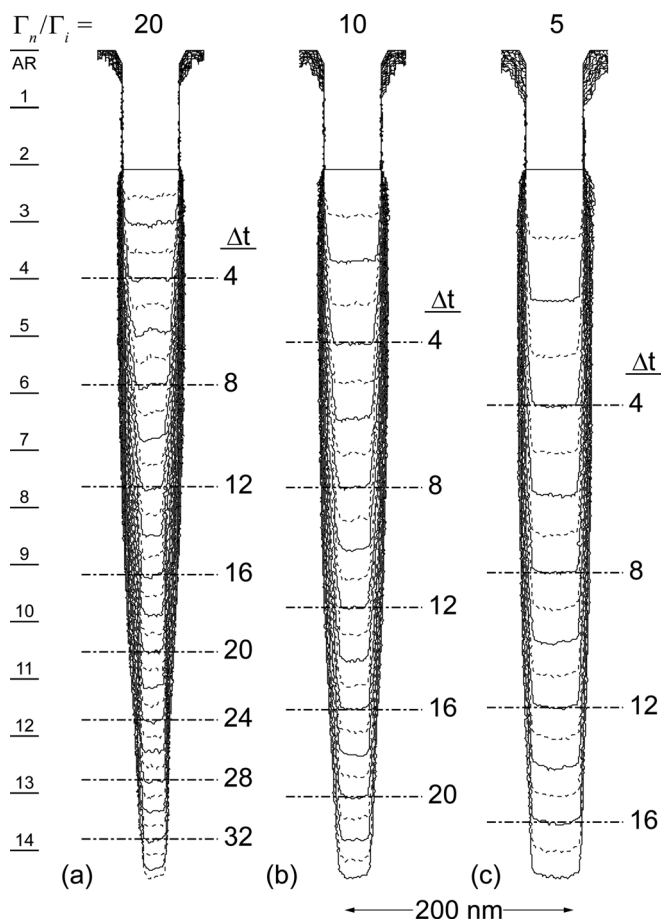


Fig. 9. Time evolution of silicon trench profile during Ar/Cl₂ etching for different neutral to ion ratios. The neutral to ion ratios are (a) 20, (b) 10, and (c) 5. Line spacing represents a constant time interval for all profiles. Numbered lines represent similar etch times in each profile.

similar trends as in the 3D structures. The large difference in etch rate when varying Γ_n/Γ_i makes it difficult to directly assess ARDE from the raw profiles, requiring us to employ the computational metrics described previously, along with normalization.

The instantaneous etch rates of the 2D trenches as a function of aspect ratio are shown in Fig. 10(a). The etch rates for each value of Γ_n/Γ_i are individually normalized to their own initial etch rate. In general, the etch rates decrease with increasing AR for all values of Γ_n/Γ_i . The etch rates for $\Gamma_n/\Gamma_i \geq 20$, though, are peaked at AR ≈ 6 , which produces a range of AR that is relatively free of ARDE. ARDE then begins at AR ≈ 6 and by AR = 10–12 the etch rate as a function of AR for $\Gamma_n/\Gamma_i \geq 20$ is similar to the smaller values of Γ_n/Γ_i . Lower values of Γ_n/Γ_i have normalized etch rates that decrease with increasing AR over the entire range studied.

Power densities, normalized to their initial values, and Cl fluxes to the etch front are shown in Fig. 10(b) as a function of AR for different values of Γ_n/Γ_i . Since the shape of the IEAD is kept constant, the average ion energies incident into the feature are also constant. Doubling the relative number of incoming ions (by halving Γ_n/Γ_i) therefore also doubles the power density at the etch front, resulting in initial power densities of 0.80, 0.39, 0.19, and 0.12 W/cm² for $\Gamma_n/\Gamma_i = 5, 10, 20$, and 30. For $\Gamma_n/\Gamma_i = 20$ and 30, cases which exhibit peaked normalized etch rates at AR ≈ 6 , the power density

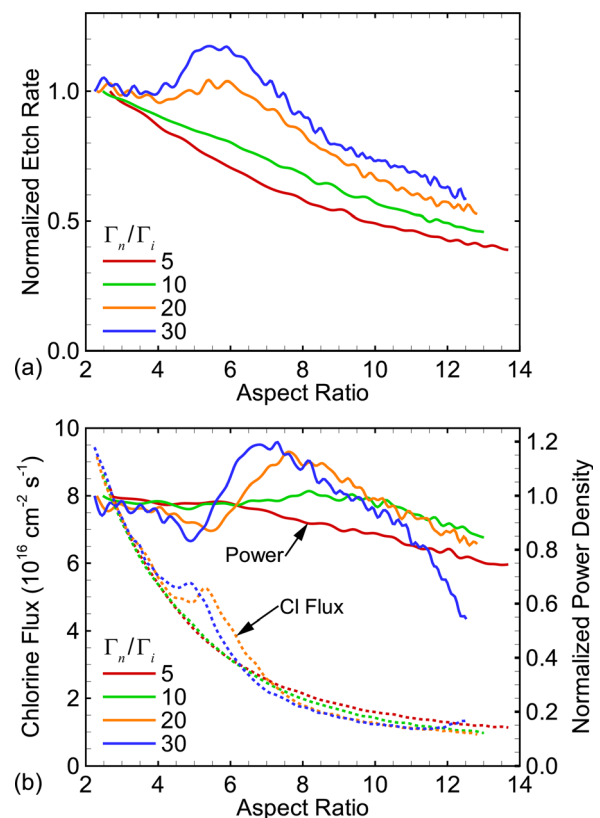


Fig. 10. (Color online) Dependence of etch rate, chlorine flux and power density on aspect ratio and the Γ_n/Γ_i ratio. Lines are labeled with neutral to ion ratios $\Gamma_n/\Gamma_i = 5, 10, 20$, and 30. (a) Etch rates normalized to the initial etch rate of each Γ_n/Γ_i . (b) Power densities (solid) and Cl flux (dotted) are measured in a small window centered in the etch front. Power density is normalized to the initial power density of each respective Γ_n/Γ_i ratio.

has a peak beginning at AR = 6. This peak in power density is due to ion funneling.

The incoming flux of chlorine atoms was held constant. The differences between chlorine fluxes to the etch front at high aspect ratios for different values of Γ_n/Γ_i are likely due to the contributions from Cl atoms that were generated by ion impact with the etch front or from the side walls. These contributions result from neutralization and subsequent thermalization of Cl^+ or the disassociation of Cl_2^+ upon impact. Since any ion incident onto the etch front will eventually thermalize (if the ion does not react), the majority of the flux of Cl^+ and a fraction of the Cl_2^+ flux will produce a source of chlorine radicals deep within the feature. These radicals can then diffuse up the feature and into the bulk gas. However, they will do so with a fairly low probability due to the low conductance of the feature at these large aspect ratios. It is more likely that the neutralized and thermalized ions will first strike the etch front before diffusing out the feature and so be included in the measurement of Cl flux. The Cl atoms originating from ions thereby appear as an additional source of Cl flux to passivate the surface. The ion flux for $\Gamma_n/\Gamma_i = 5$ is larger and so there is a larger flux of Cl atoms at high AR. The same argument can be applied to the peak in the chlorine flux occurring at AR ≈ 6 for the $\Gamma_n/\Gamma_i \geq 20$ cases. In this case, the small increase in the flux of Cl atoms is due to ions that reflect from the tapered walls and are directed into the etch front window.

The range of Γ_n/Γ_i studied here, from 5 to 30, is not inclusive of all Cl_2 etch processes. Due to the high disassociation fraction of Cl_2 at high power, Γ_n/Γ_i can be as large as several hundred.³⁸ To verify that the trends observed at lower Γ_n/Γ_i persist to a higher flux ratios, simulations were also performed at $\Gamma_n/\Gamma_i = 100$. The results indicate that the observed trends continue into this regime. The etch rate, Cl flux, and power density all appear qualitatively similar to the case of $\Gamma_n/\Gamma_i = 30$, but with more exaggerated peaking around an AR of 6. The trend of increased tapering also continues with increasing Γ_n/Γ_i , which complicates the use of our computational diagnostics. These measurement techniques are most reliable for features having relatively flat bottoms, and so do not provide consistent results as features begin to significantly taper. For the remainder of the parameters investigated here, etch conditions were limited to those which produce a relatively flat etch front up to an AR of at least 10 where neutral transport issues are expected to be most influential.

B. Chlorine recombination

The recombination of atomic Cl on surfaces to become nonreactive Cl_2 can also significantly contribute to ARDE. The initial flux of Cl atoms entering the feature is essentially isotropic, and so the view-angle to the plasma from points deep inside the feature only subtends a small fraction of the incoming neutral flux. Therefore, the vast majority of Cl atoms that reach the etch front at high aspect ratio have reflected from the inner side walls or have been emitted by the walls due to chemical reactions. There may be many such reflections prior to a Cl atom reaching the etch front.

The availability of Cl atoms at the etch front is therefore a function of the rate of surface recombination on side walls, and so ARDE will be sensitive to the recombination coefficient, S_r , of Cl atoms on the side walls. Etching of the 3D FinFET feature was simulated using values of S_r from 0.00 to 0.16; representing the range from the low recombination rate on pristine crystalline silicon to values close to that of poly-Si at room temperature.¹⁸ The resulting profiles are shown in Fig. 11 for $S_r = 0.00, 0.04$, and 0.16, and suggest that radical recombination on side walls does indeed have a significant effect on ARDE for these conditions. Profiles are shown at two etch times, t_1 , approximately half-way through the etch, and t_2 , at the end of the etch. The profile having $S_r = 0$ has little difference in etch depth between inside the trenches and the open field, indicating there being little ARDE. However, profiles having S_r as small as 0.04 already show some evidence of ARDE at t_1 . By time t_2 , significant differences in etch depth between the open field and the trenches are evident for both $S_r = 0.04$ and 0.16. The etch rate of an unpatterned wafer is not expected to have a dependence on S_r . Without patterning, none of the impinging Cl atoms would have interacted with surfaces prior to striking the etch front. Therefore, the differences in etch depth at t_2 as a function of S_r in the quasiopen field (200 nm gap) between the arrays of fins indicates that ARDE occurs even for the modest AR (≈ 3.5) in this region. Other than the aspect ratio dependence of the etch rates, the resulting profiles are similar for different values of S_r .

To better quantify the consequences of radical recombination on neutral transport and separate these effects from 3D transport issues, profiles were simulated for infinite trenches having a width of 50 nm for the same range of recombination probabilities. The resulting profiles are shown in Fig. 12. The profiles show that smaller recombination probabilities produce more tapered features at the same aspect ratio while having a higher etch rate. These trends result, in part, from the etching in high AR features being neutral starved, and so

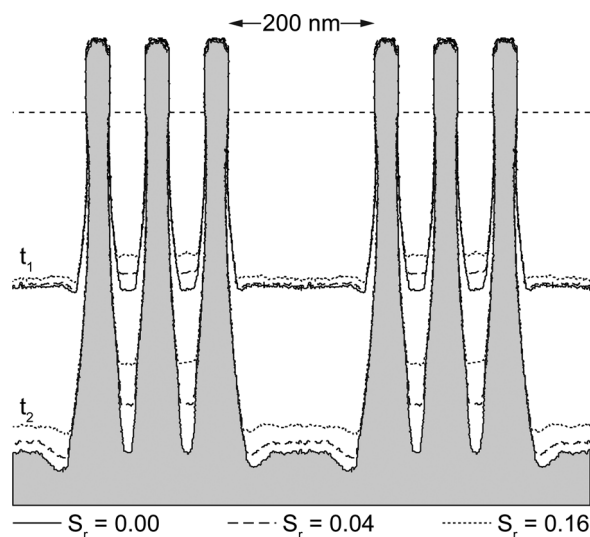


Fig. 11. Two dimensional slice through fin profile for several surface recombination probabilities, S_r . The lines labeled t_1 and t_2 represent equal etch times. The slice is taken through the center of the length of the fin.

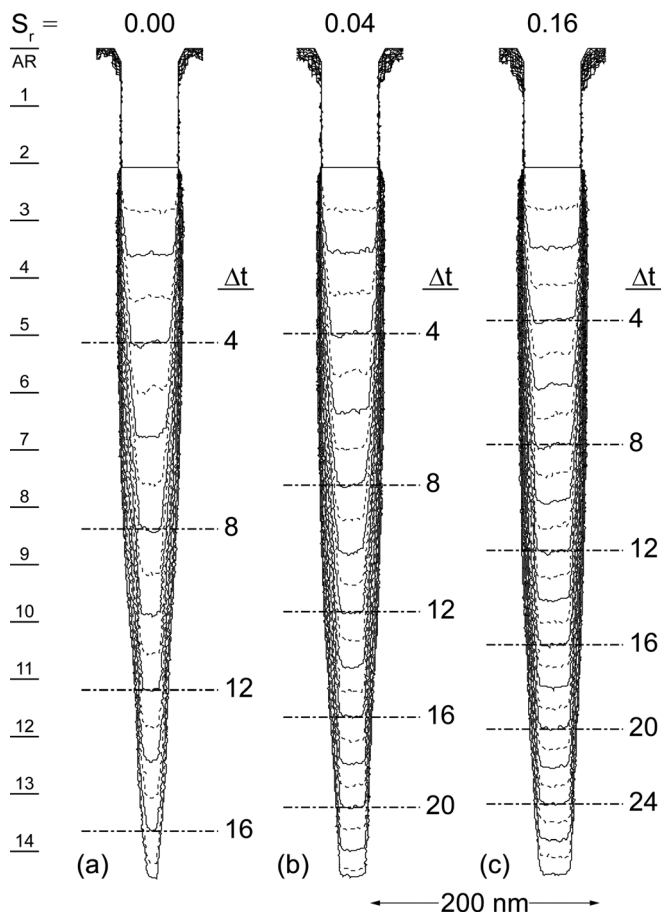


FIG. 12. Time evolution of silicon trench profile during Ar/Cl₂ etching for different chlorine recombination probabilities, S_r . The recombination probabilities of atomic Cl on SiCl₃ shown are (a) 0.00, (b) 0.04, and (c) 0.16. Line spacing represents a constant time interval Δt for all profiles. Numbered lines represent similar etch times in each profile.

any process that increases the flux of Cl atoms to the etch front will increase the rate of etching.

The instantaneous normalized etch rates for these features are shown in Fig. 13(a) as a function of the aspect ratio. Etch rates for different values of S_r are all normalized to the open-field etch rate of the base case ($S_r = 0.08$). These etch rates have significantly different responses to varying S_r at low and high aspect ratios. At low aspect ratios ($AR < 7$), there is a direct correlation between the recombination rate and ARDE—larger recombination probabilities produce an etch rate which is more strongly dependent on aspect ratio than lower recombination probabilities. For the limiting case of $S_r = 0.0$, which is likely unphysical on any real material, there is an increase in the etch rate above the open field rate between $AR = 5-7$. This increase in etch rates correlates to the onset of ion funneling, and so is probably more related to geometry, the particular slopes of the side wall and our method of measuring etch rate, rather than an actual inverse ARDE. However, there is a clear trend that low probabilities of recombination are less sensitive to ARDE. At high aspect ratios ($AR > 10$), all etch rates show a similar dependence on the aspect ratio, despite having different absolute values.

The Cl atom fluxes and power densities onto the etch front as a function of AR are shown in Fig. 13(b) for

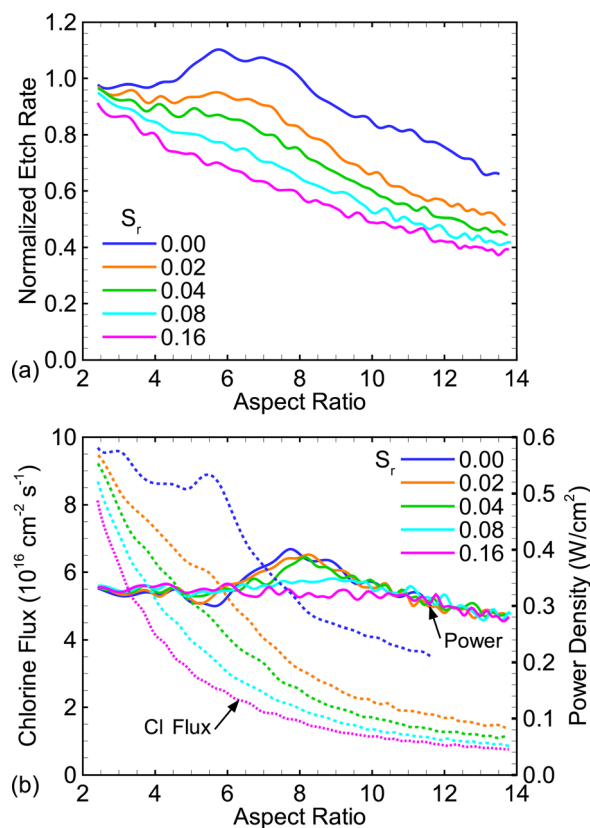


FIG. 13. (Color online) Dependence of (a) etch rate, and (b) chlorine flux and power density on aspect ratio and the probability of recombination of radical chlorine on the walls, S_r . (a) Etch rates are normalized to the etch rate in the open field for the base case ($S_r = 0.08$). Power density and chlorine flux are measured at the etch front as it evolves.

different values of S_r . There is a strong correlation between the chlorine flux and ARDE—higher values of Cl fluxes (lower values of S_r) at lower AR correspond to higher etch rates. The power flux remains nearly constant throughout the etch, with the exception of a small peak between $AR = 8-9$. This peak is related to ion funneling as the features begin to taper. Similar to the etch rate, for small aspect ratios ($AR < 7$) larger recombination probabilities have lower chlorine fluxes to the etch front. Perhaps more important, the change in chlorine flux with aspect ratio is also greater for larger recombination probabilities, leading directly to ARDE. At higher aspect ratios, larger recombination probabilities still reduce the chlorine flux to the etch front, but the dependence on aspect ratio is similar between the different recombination rates, indicating that some other physical process is influencing neutral transport at these ARs.

(The Cl flux and power density for $S_r = 0$ and $AR > 12$ are omitted from Fig. 13(b). This omission is due to our measurement technique becoming susceptible to statistical variation when features become highly tapered. This issue only affects the measurement of fluxes but does not significantly affect measurements of the etch rate.)

C. Neutral angular distribution

One possible method to decouple neutral transport issues from aspect ratio is to produce neutral reactant fluxes having

an anisotropic angular distribution. As Coburn and Winters suggested, if the incoming neutral flux was perfectly anisotropic then the neutral flux onto the etch front would actually increase with increasing aspect ratio.⁶ This scaling results from all incoming neutrals striking the bottom of the feature while the etch front only consumes a fraction of those based on there being a small reactive sticking coefficient, S_n . The Cl atoms that do not react with the etch front must diffuse back up the feature to return to the bulk gas. As the aspect ratio increases, the conductance of the tube decreases, resulting in an increased probability that the Cl atoms reflecting from the etch front will also be reflected off the side walls back down to the etch front. While a perfectly anisotropic neutral flux would be difficult to produce, some degree of anisotropy in the neutral flux can be produced by techniques such as neutral beam etching where neutrals are produced by grazing angle collision of anisotropic ions.³⁹⁻⁴¹

To assess the consequences of anisotropic neutral fluxes on ARDE, the initial angle with respect to the vertical of each neutral pseudoparticle was linearly scaled by the factor γ_n . The naturally occurring isotropic angular distribution has $\gamma_n = 1$, while values smaller than one represent a narrowed neutral angular distribution. The resulting profiles for the 2D trenches for $\gamma_n = 1, 0.5$, and 0.25 are shown in Fig. 14.

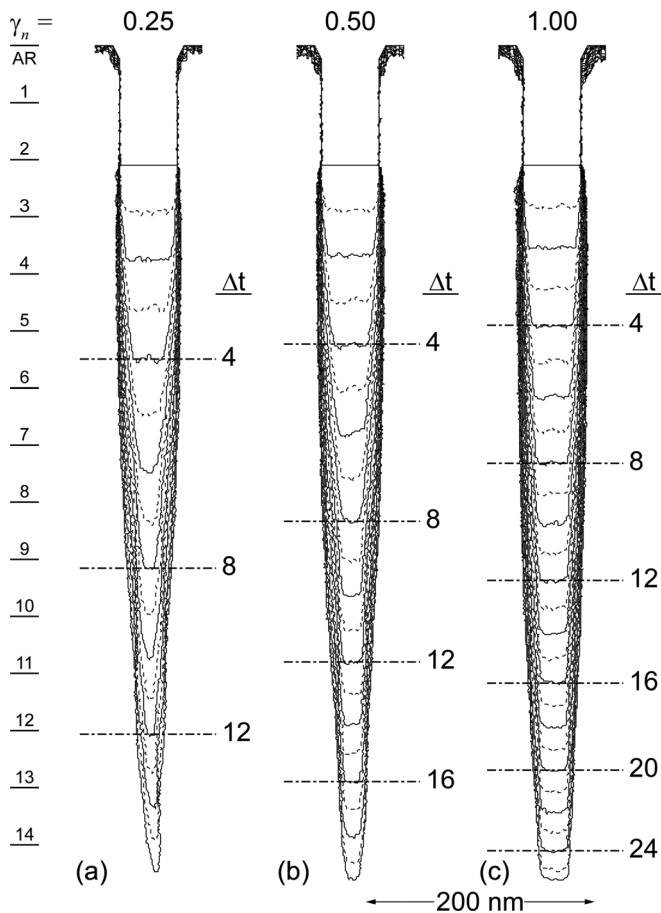


FIG. 14. Time evolution of silicon trench profile for different neutral angular distributions, γ_n . The normalized angular distribution scaling factors are (a) 0.25, (b) 0.50, and (c) 1.00. Line spacing represents a constant time interval Δt for all profiles. Numbered lines represent similar etch times in each profile.

Smaller values of γ_n produce higher etch rates due to the increased neutral flux to the etch front, but the profiles also have significantly more tapering. The side wall chlorination just above the etch-front for $\gamma_n = 0.25$ is 2.1 Cl atoms/site. This value is only slightly lower than for the base case (2.2 Cl atoms/site). One might expect a significantly lower Cl passivation on the side walls for the anisotropic Cl flux as there would be fewer collisions on the side wall. The higher than expected chlorination results from Cl isotropically reflecting from other surfaces, tempered by the larger number of primary ions striking on the more tapered side walls.

The normalized etch rate, chlorine flux, and power density at the etch front as a function of AR for different values of γ_n are shown in Fig. 15. While there is significantly more chlorine reaching the etch front with narrower neutral angular distributions, the neutral flux retains a significant dependence on the aspect ratio. The resulting normalized etch rate for $\gamma_n = 0.25$ has a peak at an aspect ratio of ≈ 6 . The etch rate for $\gamma_n = 0.50$ appears to have a mild peak in the same range of AR, producing a process window having quasi ARDE-free behavior. Power density is essentially constant compared to the Cl flux over the range of aspect ratios investigated. (Note that, power density and chlorine fluxes are omitted for $\gamma_n = 0.25$ with $AR > 10$ due to the highly tapered profile, as discussed previously.)

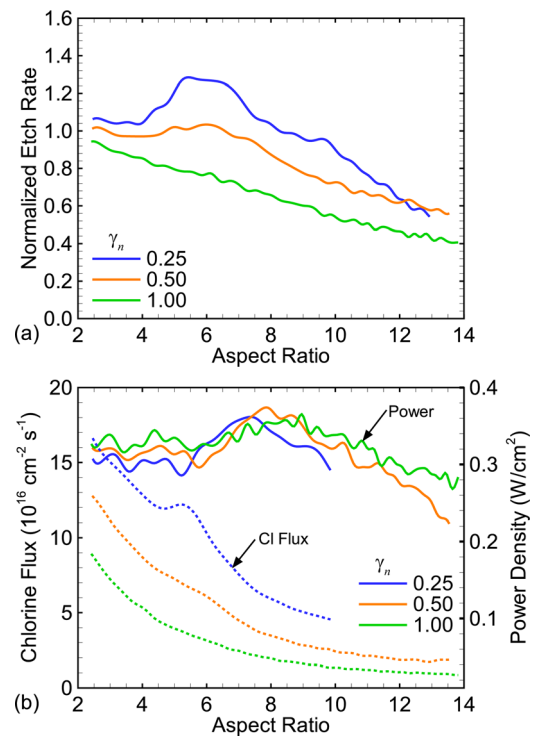


FIG. 15. (Color online) Dependence of (a) etch rate, and (b) chlorine flux and power density on aspect ratio and the angular distribution of neutrals, γ_n . Etch rate is normalized to the etch rate in the open field for the base case ($\gamma_n = 1.00$). Power density and chlorine flux are measured at the etch front as it evolves. Chlorine flux and power density are omitted above an AR of 10 for $\gamma_n = 0.25$ due to the highly tapered profile interfering with the measurement technique.

D. Ion angular distribution

While previous cases more directly address details of the neutral transport, it is also possible that ion shadowing can contribute to ARDE, and even have a second order effect on neutral transport through, for example, removing Cl atoms from the side walls. By artificially varying the angular distribution of ions in the simulation, the contribution of ion shadowing to ARDE can be assessed. Changing process conditions, such as bias voltage, to narrow (or broaden) the IEAD unfortunately also produces changes in the magnitudes of fluxes of both neutrals and ions. Instead, a linear scaling factor, γ_i , was used similarly to the neutral fluxes, to narrow or broaden the angular distribution of ions obtained from the base case of the reactor scale model.

Etch profiles for $\gamma_i = 0.25$ to 1.5, with $\gamma_i = 1$ representing the base case, are shown in Fig. 16. Values of $\gamma_i < 1$ are narrower distributions than the base case and values of $\gamma_i > 1$ are wider. The average ion angular distribution of the base case is $\pm 2.2^\circ$; therefore, $\gamma_i = 0.25$ results in an average ion angle distribution of $\pm 0.55^\circ$ and $\gamma_i = 1.5$ yields an angular spread of $\pm 3.3^\circ$. The resulting etch profiles have differences in side wall slope, extending to bowing, but fairly similar integrated etch rates. Narrower angular distributions produce

more tapered side wall profiles than the base case (18% reduction in width at half etch height for $\gamma_i = 0.25$ compared to the base case). At the other extreme, the profile resulting from $\gamma_i = 1.5$ has increased side wall bowing (30% increase in width at half etch height compared to the base case). The broader ion angular distributions enable sites having off normal view-angles to the plasma to intercept a larger fraction of the incoming ion flux, the first consequence being bowing under the mask. Once this initial bowing occurs, ions specularly reflecting from the bowed surface are more likely to strike the side wall deeper in the trench. Therefore, the maximum in bowing occurs at deeper locations in the trench that do not have large view-angles to the plasma.

In spite of the differences in side wall slope and bowing, there is little difference in etch rate until an aspect ratio of 6–7, at which time larger values of γ_i have smaller etch rates. These trends are shown more quantitatively in Fig. 17 where normalized etch rates, Cl fluxes, and power densities are shown as a function of aspect ratio for different values of γ_i . The ion angular distributions for all γ_i have similar sensitivity to ARDE, a predominantly (negative) linear dependence of etch rate on aspect ratio over the entire range studied, but slightly steeper slopes (more sensitive to ARDE) for the wider angular distributions. While the overall trends in the etch rate are similar for different values of γ_i , the small differences in etch rate, when integrated over a large range of

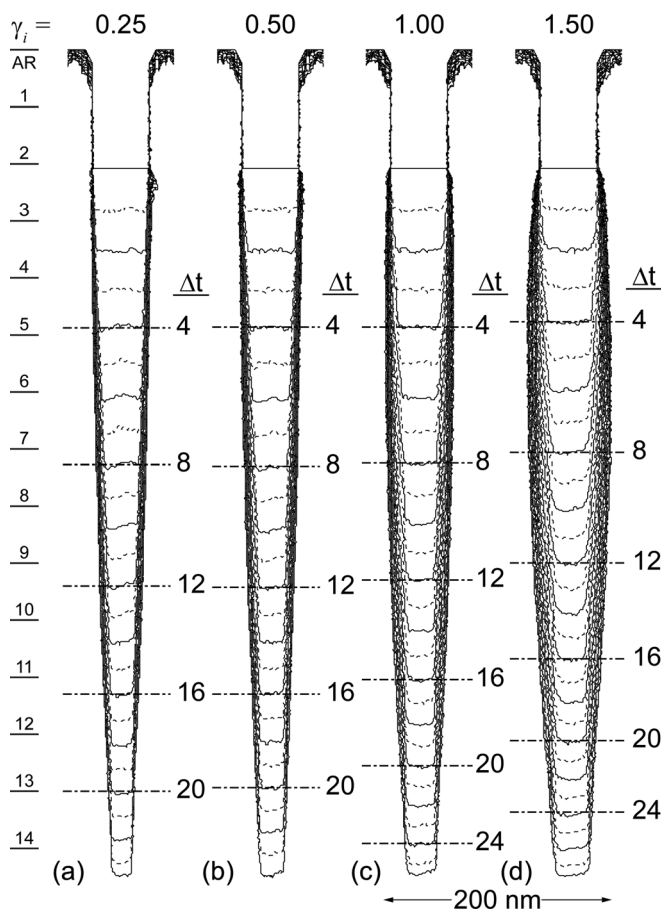


FIG. 16. Time evolution of silicon trench profile for different ion angular distributions, γ_i . The normalized angular distribution scaling factors shown are (a) 0.25, (b) 0.50, (c) 1.00, and (d) 1.50. Line spacing represents a constant time interval Δt for all profiles. Numbered lines represent similar etch times in each profile.

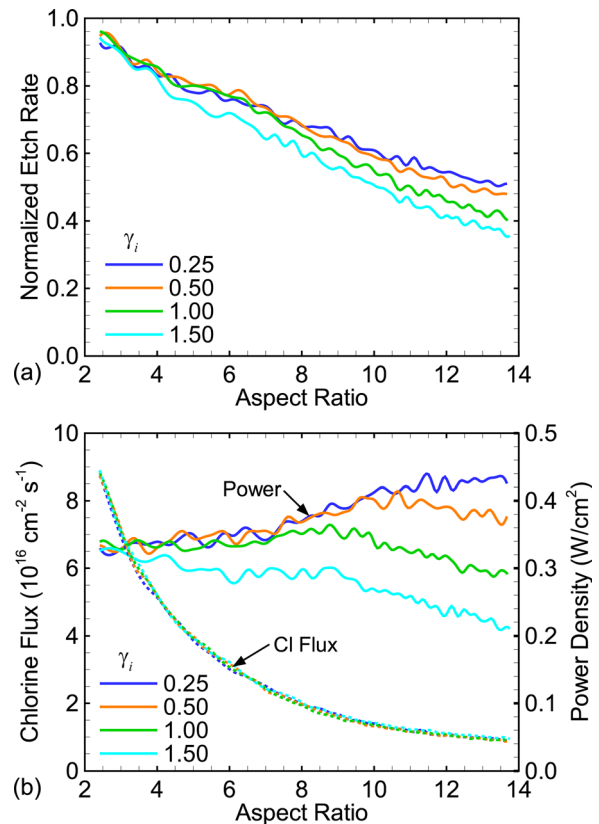


FIG. 17. (Color online) Dependence of (a) etch rate, and (b) chlorine flux and power density on aspect ratio and the angular distribution of ions, γ_i . Etch rates are normalized to the etch rate in the open field for the base case ($\gamma_i = 1.00$). Power density and chlorine flux are taken at the etch front as it evolves.

aspect ratio, produces significant differences in etch depth. These trends indicate that ion shadowing does affect ARDE, but its contributions are relatively small compared to the consequences of neutral transport.

The chlorine flux incident onto the etch front is essentially insensitive to the angular distribution of the ions. Power density, however, monotonically decreases for broader distributions (larger values of γ_i) and particularly so for larger values of AR. These trends indicate that the average sticking coefficient of neutrals on the etch front, S_n , is not significantly changed by modulation in the power density for these process conditions, as is implied by the synergy model.¹⁰

E. Dependence on feature width

One of the defining characteristics of ARDE is that the etch rate depends only on aspect ratio and not necessary on the absolute CD of the etched feature, generally the width of the feature. Other profile parameters, such as the loss of CD due to tapering, have been shown to be dependent on view angle to the plasma.⁴² While the two-dimensional view angle to the plasma is related to AR, the correlation of loss of CD to view angle suggests a sensitivity to reactive fluxes that directly arrive at a surface site. To determine if the etch rate of simple structures using this reaction mechanism is related to AR, CD, or view angle, etch profiles were simulated for three trench widths of 33, 50, and 67 nm. The resulting normalized etch rates for two values of chlorine recombination probabilities (S_r) are shown in Fig. 18. With $S_r = 0.08$, the base case, the etch rate depends only on the aspect ratio with only small differences between the different trench widths that are likely statistical in nature. The etch rate in the absence of recombination of chlorine on the walls, $S_r = 0$, is nearly the same for all trench widths for small AR (<4) and large AR (>9). At intermediate values of AR (4–9), the etch rate is sensitive to the width of the feature.

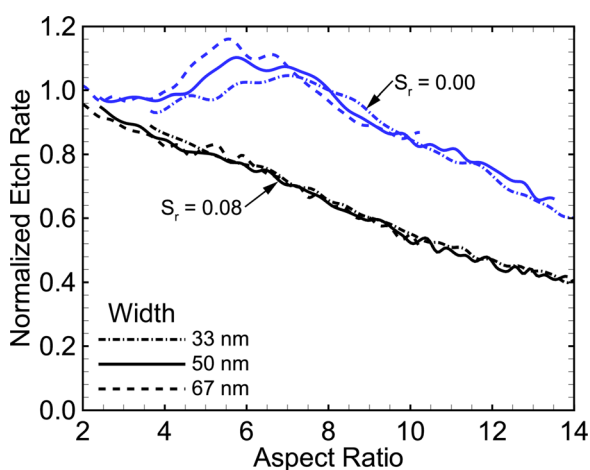


Fig. 18. (Color online) Etch rate as a function of aspect ratio and trench width for two values of chlorine recombination rate, S_r . For the base case, $S_r = 0.08$, the etch rate depends only on aspect ratio and not trench width. For the case without chlorine recombination, $S_r = 0.00$, the peak in etch rate weakly depends on trench width, but at higher aspect ratios the ARDE trends are again independent of trench width.

These results imply that the local peaking in etch rates observed in many of these parameterization are likely related to fine details of the evolution of the feature that may depend on critical dimension. The technique used here to measure the etch rate, described in Sec. IID, is based on the change in height of the profile within a small area at the center of the feature. This technique may somewhat exaggerate the severity of the peaks in the etch rate which are driven by geometry dependent ion funneling. The total number of silicon atoms removed per second, for instance, shows a similar decrease with the aspect ratio, but does not exhibit the peaking as observed in the calculated etch rate.

F. Parameters affecting ARDE

The results of this computational investigation suggest that a dominant cause of ARDE is the decrease in neutral radical flux reaching the etch front with increasing AR, provided the process is not already in a neutral saturated regime. By increasing the neutral radical flux relative to the ions, the surface at the etch front becomes more passivated, and so the etch rate is less sensitive to modest changes to the neutral flux that may occur with aspect ratio. These trends have been experimentally observed.^{15,30} The available experimental data indicating that large values of neutral-to-ion flux ratio produces a saturation in the etch rate were predominantly obtained from measurements in the open field (nonpatterned wafers). Although these data have provided extremely important insights, the data do not address the possible coupling of neutral and ion fluxes that may occur within features. In this study, changes in system parameters that increased the neutral flux to the etch front relative to the ion flux (e.g., reducing the recombination of radicals on the feature walls, increasing the neutral to ion ratio in the incoming fluxes, or employing an anisotropic flux of neutral radicals) all reduced ARDE but also produced more tapered features.

The onset of tapering of the feature at an AR of 6–8 is correlated with a decrease in chlorine radical flux to the etch front as well as with the etch rate. This correlation between tapered features and reduced neutral transport could be due to several different mechanisms. The first is the reduction in conductance of neutral particles due to the angle of the surface normal in the tapered region. Since the solid-angle normalized probability of emission or reflection for a Lambertian angular distribution is maximum along the surface normal, neutral species which diffuse down to the tapered region of the feature are preferentially directed back up the feature as the angle of the taper increases.

Another factor which contributes to the decrease in neutral flux at the etch front in tapered features is the erosion of side wall passivation and the subsequent repassivation of the exposed silicon site. Due to the flux of ions being anisotropic, the tapered side walls are exposed to higher fluxes of ions than strictly vertical side walls. While our reaction mechanism includes an angular dependence to the sputter reactions, which goes to zero at grazing angles, there is still a finite probability on the tapered walls. The effect of this side wall scattering is shown in the results of Fig. 6, where

the number of chlorine atoms per Si site decreases from 2.8 to 2.2 as the tapering becomes more severe. This erosion of the side wall exposes bare silicon sites which will consume incoming Cl flux through passivation, which in turn reduces the neutral flux in the etch front of a tapered feature.

The synergy model of Gottscho *et al.* predicts that there is a coupling between the ion and neutral fluxes such that changing the incoming ion flux can change the neutral flux to surfaces deep in the feature with no change in the neutral flux entering the feature.¹⁰ This process occurs due to the ion flux changing the steady state surface chlorine coverage on the etch front, which changes S_n . The change in S_n then impacts the neutral flux through Eq. (1). Since the tapering of the side walls affects the ion flux at the etch front through ion funneling, it is possible that the synergy coupling may also modulate neutral flux to the etch front as a function of side wall taper. Our results do not indicate that this effect is strongly influencing the neutral flux or etch rate for this reaction mechanism. The power densities and chlorine fluxes, shown in Fig. 17(b) for a range of γ_i , display a doubling of power density from $\gamma_i = 1.5$ to $\gamma_i = 0.25$, but no discernable decrease in measured Cl flux at the etch front.

While increasing the neutral radical flux to the etch front does not eliminate ARDE over all ARs investigated here, it is possible to postpone the onset of ARDE. For example, when varying the recombination probability of Cl atoms on the side walls [see Fig. 13(a)], there were ranges of AR where ARDE was not significant. For these ranges of AR, the feature has not yet formed any significant taper, and so is able to benefit from the higher neutral flux as predicted by analytical models. A similar trend occurs when narrowing the angular distribution of the neutrals. For example, etch rates with $\Gamma_n/\Gamma_i = 20$ [Fig. 10(a)] and $\gamma_n = 0.5$ [Fig. 15(a)] are not sensitive to ARDE for AR as large as 8.

The results of our investigation indicate that issues related to the transport of radicals from the bulk plasma into the feature dominate ARDE for the conditions studied here. That is, there are surface reactions that are rate limited by the availability of neutral radical fluxes and reactions that are rate limited by ion fluxes. Differences in substrate temperature, operating pressure, or ion energies may affect ARDE behavior by their influence on reactions initiated by neutral or radical fluxes. However, in general, for the etch rate to depend on AR, either the neutral or ion flux reaching the etch front must also depend on AR. For the reaction mechanism used here, the strongest AR dependence originates from the change of the neutral conduction with AR. For other reaction mechanisms or operating conditions, the transport of neutral etch products out of the feature may dominate ARDE due to redeposition. However, in both scenarios, it is the dependence of neutral transport on AR which result in ARDE.

IV. CONCLUDING REMARKS

Aspect ratio dependent etching remains a challenge to optimizing feature profiles during plasma etching, a situation that has become more critical with the introduction of 3D structures such as FinFETs. In this investigation of etching

of Si in Ar/Cl₂ gas mixtures, the majority of ARDE arises from issues related to neutral transport. Several factors were varied that affect neutral transport, including surface recombination of radicals, neutral-to-ion flux ratios, critical dimension, 3D geometry, and neutral angular distribution. A general conclusion of this work is that any reaction that relies on a flux of neutral species from the bulk gas will, to some degree, suffer from ARDE. However, some trade-offs can be made to change the dependence on the aspect ratio. Increasing neutral flux to the etch front may produce a quasi-aspect ratio independent regime of etching for low and moderate aspect ratios. Doing so may involve a trade-off with a greater propensity for tapered features, and increased ARDE outside of this aspect ratio independent window.

The details of the results of this investigation depend on the details of the reaction mechanism. Etching of dielectrics, such as SiO₂ and Si₃N₄, has more complex reaction mechanisms based on the use of fluorocarbon containing gas mixtures.^{43–45} In dielectric etching, the etch rate is sensitive to the thickness of the fluorocarbon polymer layer on the etch front and the etch process requires multiple steps. (That is, a Si₃N₄ unit is not necessarily removed with a single strike of an ion.) The end result is that the dependence of etch rate on the ratio of passivating neutral and ion fluxes, and their angular distributions, is more complex. For example, in the Si etch mechanism described here, increasing Cl fluxes to the etch front typically reduces ARDE. In the dielectric etch mechanism, increasing fluorocarbon fluxes to the etch front can increase etch rates over a limited range of Γ_n/Γ_i , beyond which etch rates may decrease (or terminate—an etch stop) due to thickening of the passivation layer. With those caveats, based on results from preliminary numerical investigations of ARDE in fluorocarbon containing plasmas, the same general trends discussed here appear to be valid.

Remembrance of Harold Winters

One of the authors, MJK, very early in his career faced a professional crisis. Seeking guidance, he was counseled to write to the most respected scientists in the field and ask for their advice. (This was before the days of e-mail.) The obvious choices were Harold Winters and John Coburn. Given that he was totally unknown to Harold and John, MJK was reluctant to write to them, sending the equivalent of junk mail, but in the end, he did send a letter. About a week later, Harold and John called MJK. They had received the letter and had invested considerable time discussing the issue. This was quite a surprise to MJK—who would respond to a complete unknown simply because he wrote a letter? Harold and John did so because they felt it important to mentor young researchers. Harold and John then spent about an hour speaking with MJK, providing what may have been career saving advice. This sincere and heartfelt (and time consuming) advice from Harold was given to an unknown young scientist, simply because he asked. MJK has been and will continue to be grateful for having received such mentoring and excellent advice.

ACKNOWLEDGMENTS

This work was supported by Lam Research Corporation and the Department of Energy Office of Fusion Energy Science (DE-SC000319, DE-SC0014132).

- ¹C. G. N. Lee, K. J. Kanarik, and R. A. Gottscho, *J. Phys. D: Appl. Phys.* **47**, 273001 (2014).
- ²G. S. Oehrlein, R. J. Phaneuf, and D. B. Graves, *J. Vac. Sci. Technol., B* **29**, 10801 (2011).
- ³O. Joubert *et al.*, *Proc. SPIE* **8328**, 83280D (2012).
- ⁴L. Meng, J. Li, C. Zhao, and J. Yan, *ECS Solid State Lett.* **3**, Q25 (2014).
- ⁵R. L. Bates, M. J. Goeckner, and L. J. Overzet, *J. Vac. Sci. Technol., A* **32**, 51302 (2014).
- ⁶J. W. Coburn and H. F. Winters, *Appl. Phys. Lett.* **55**, 2730 (1989).
- ⁷A. Beskok and G. E. Karniadakis, *Microscale Thermophys. Eng.* **3**, 43 (1999).
- ⁸F. Celestini and F. Mortessagne, *Phys. Rev. E* **77**, 21202 (2008).
- ⁹W. Steckelmacher, *Rep. Prog. Phys.* **49**, 1083 (1986).
- ¹⁰R. A. Gottscho, C. W. Jurgensen, and D. J. Vitkavage, *J. Vac. Sci. Technol., B* **10**, 2133 (1992).
- ¹¹A. P. Mahorowala and H. H. Sawin, *J. Vac. Sci. Technol., B* **20**, 1064 (2002).
- ¹²Y. Osano and K. Ono, *J. Vac. Sci. Technol., B* **26**, 1425 (2008).
- ¹³J. S. Han, J. P. McVittie, and J. Zheng, *J. Vac. Sci. Technol., B* **13**, 1893 (1995).
- ¹⁴J. Hoang, C.-C. Hsu, and J. P. Chang, *J. Vac. Sci. Technol., B* **26**, 1911 (2008).
- ¹⁵J. A. Levinson, E. S. G. Shaqfeh, M. Balooch, and A. V. Hamza, *J. Vac. Sci. Technol., A* **15**, 1902 (1997).
- ¹⁶P. Clausing, *J. Vac. Sci. Technol.* **8**, 636 (1971).
- ¹⁷A. D. Bailey, M. C. M. van de Sanden, J. A. Gregus, and R. A. Gottscho, *J. Vac. Sci. Technol., B* **13**, 92 (1995).
- ¹⁸G. P. Kota, J. W. Coburn, and D. B. Graves, *J. Vac. Sci. Technol., A* **16**, 270 (1998).
- ¹⁹Y. Zhang, M. J. Kushner, S. Sriraman, A. Marakhtanov, J. Holland, and A. Paterson, *J. Vac. Sci. Technol., A* **33**, 31302 (2015).
- ²⁰M. J. Kushner, *J. Phys. D: Appl. Phys.* **42**, 194013 (2009).
- ²¹Y. Zhang, C. Huard, S. Sriraman, J. Belen, A. Paterson, and M. J. Kushner, *J. Vac. Sci. Technol., A* **35**, 21303 (2017).
- ²²H. D. Hagstrum, *Phys. Rev.* **122**, 83 (1961).
- ²³C. C. Cheng, K. V. Guinn, V. M. Donnelly, and I. P. Herman, *J. Vac. Sci. Technol., A* **12**, 2630 (1994).
- ²⁴N. Layadi, V. M. Donnelly, and J. T. C. Lee, *J. Appl. Phys.* **81**, 6738 (1997).
- ²⁵M. W. Radny, P. V. Smith, and P. L. Cao, *Surf. Sci.* **365**, 15 (1996).
- ²⁶R. Khare, A. Srivastava, and V. M. Donnelly, *J. Vac. Sci. Technol., A* **30**, 51307 (2012).
- ²⁷G. Cunge, D. Vempaire, R. Ramos, M. Touzeau, O. Joubert, P. Bodard, and N. Sadeghi, *Plasma Sources Sci. Technol.* **19**, 34017 (2010).
- ²⁸M. Balooch, M. Moalem, W.-E. Wang, and A. V. Hamza, *J. Vac. Sci. Technol., A* **14**, 229 (1996).
- ²⁹J. P. Chang and H. H. Sawin, *J. Vac. Sci. Technol., A* **15**, 610 (1997).
- ³⁰J. P. Chang, J. Arnold, G. Zau, H.-S. Shin, and H. H. Sawin, *J. Vac. Sci. Technol., A* **15**, 1853 (1997).
- ³¹M. E. Barone and D. B. Graves, *Plasma Sources Sci. Technol.* **5**, 187 (1996).
- ³²J. M. Lane, K. H. A. Bogart, F. P. Klemens, and J. T. C. Lee, *J. Vac. Sci. Technol., A* **18**, 2067 (2000).
- ³³G. Cunge, M. Kogelschatz, and N. Sadeghi, *J. Appl. Phys.* **96**, 4578 (2004).
- ³⁴G. Cunge, R. L. Inglebert, O. Joubert, L. Vallier, and N. Sadeghi, *J. Vac. Sci. Technol., B* **20**, 2137 (2002).
- ³⁵C. Petit-Etienne, M. Darnon, P. Bodart, M. Fouchier, G. Cunge, E. Pargon, L. Vallier, O. Joubert, and S. Banna, *J. Vac. Sci. Technol., B* **31**, 11201 (2013).
- ³⁶M. A. Vyvoda, H. Lee, M. V. Malyshev, F. P. Klemens, M. Cerullo, V. M. Donnelly, D. B. Graves, A. Kornblit, and J. T. C. Lee, *J. Vac. Sci. Technol., A* **16**, 3247 (1998).
- ³⁷M. A. Vyvoda, M. Li, D. B. Graves, H. Lee, M. V. Malyshev, F. P. Klemens, J. T. C. Lee, and V. M. Donnelly, *J. Vac. Sci. Technol., B* **18**, 820 (2000).
- ³⁸N. C. M. Fuller, I. P. Herman, and V. M. Donnelly, *J. Appl. Phys.* **90**, 3182 (2001).
- ³⁹S. Samukawa, K. Sakamoto, and K. Ichiki, *Jpn. J. Appl. Phys., Part 2* **40**, L779 (2001).
- ⁴⁰S. Noda, H. Nishimori, T. Ida, T. Arikado, K. Ichiki, T. Ozaki, and S. Samukawa, *J. Vac. Sci. Technol., A* **22**, 1506 (2004).
- ⁴¹S. Samukawa, *Jpn. J. Appl. Phys., Part 1* **45**, 2395 (2006).
- ⁴²N. Kuboi, T. Tatsumi, M. Fukasawa, T. Kinoshita, J. Komachi, H. Ansai, and H. Miwa, *J. Vac. Sci. Technol., A* **31**, 61304 (2013).
- ⁴³X. Li, X. Hua, L. Ling, G. S. Oehrlein, M. Barela, and H. M. Anderson, *J. Vac. Sci. Technol., A* **20**, 2052 (2002).
- ⁴⁴M. J. Barela, H. M. Anderson, and G. S. Oehrlein, *J. Vac. Sci. Technol., A* **23**, 408 (2005).
- ⁴⁵O. Joubert, G. S. Oehrlein, and M. Surendra, *J. Vac. Sci. Technol., A* **12**, 665 (1994).